Laser-Based Additive Manufacturing and Mechanical Surface Post-Processing: Comparison of Barrel Finishing, Shot and Ultrasonic Peening for Corrosion Resistance Improvement of Superalloy

D. A. Lesyk[1,2,3] · B. N. Mordyuk[2] · S. Martinez[3] · V. V. Dzhemelinskyi[1] ·
D. Grzesiak[4] · D. Grochała[4] · A. Lamikiz[3,5]

Abstract

Nickel-based alloy test parts were manufactured using an industrial laser 3D printing system. The corrosion behavior of the laser powder bed fused (LPBF) Inconel 718 alloy parts are analyzed in as-built and mechanical surface post-processed conditions, i.e. after barrel finishing, shot peening, ultrasonic shot peening, and multipin ultrasonic impact treatment. The microstructural features are analyzed using the X-Ray diffraction (XRD) analysis and scanning electron microscopy (SEM) / energy dispersive spectroscopy (EDS) methods. The open circuit potential and linear/cyclic polarization were registered in a 3.5 wt.% NaCl solution. The surface roughness diminishment, defects elimination, residual pores' closure, as well as the residual stress and structure-phase state changes were under special attention. The polarization resistance, corrosion current density, corrosion rate, pitting initiation rate, anodic dissolution, ability for repassivation, and crevice corrosion resistance were assessed and compared.

Introduction

The nickel-based superalloys are used for a specific range of applications due to their ability to withstand loading at a severe/hot operating temperature and a substantial resistance to mechanical degradation over extended periods of time. Inconel 718 (IN 718) alloy is a special type of high-strength superalloy with a nickel-chrome base that makes it resistant to corrosion, high pressure, and extreme temperatures of up to 700°C [1]. Moreover, the IN 718 superalloy has an intrinsic ability to provoke

---

Extended author information available on the last page of the article

a strong and stable protective oxide layer when exposed to heat. This natural passivation feature formed by chromium and aluminum protects the material against damage and corrosion. Because of its unique properties, the IN 718 alloy is one of the most widely used nickel-based alloys in extreme heat applications, such as turbojet engine parts (compressor casings, discs, and fan blades) in the aerospace industry and nuclear reactor parts in nuclear application, as well as oil drilling shafts in oil and gas exploration. The conventional processing route for the nickel-based IN 718 alloy is casting followed by heat treatment and final machining. At the same time, the conventional manufacturing techniques for the IN 718 alloy end-products are complicated in processing routes, especially for the production of complexly shaped parts.

Nowadays, IN 718 alloy is associated with metal additive manufacturing, in which the powder material is added layer by layer contrary to formative and subtractive manufacturing [2]. Moreover, the complexly shaped metal parts can be built by 3D printing in a shorter time with lesser waste production [3, 4]. Advanced 3D printing techniques, such as direct energy deposition and powder bed fusion technologies are currently applied to produce the IN 718 alloy end-products with the required properties. Compared to the powder bed fusion techniques (laser or electron beam powder bed fusion, and binder jetting), the geometrical accuracy and detail resolution are lower in the metal parts printed by the direct energy deposition techniques (plasma or electric arc metal deposition and electron beam or laser metal deposition) [2, 5]. As a result, the direct energy deposition techniques are mostly used for repairing/coating the metal parts with a simple geometric shape through the application of support structure limits.

The laser powder bed fusion (LPBF) technique is one of the most innovative 3D printing technologies for the manufacturing of the IN 718 alloy end-products, producing almost 100% dense components [6–8]. The parts printed by LPBF consist of highly different microstructures (cellular and columnar grains of austenitic matrix phase γ coupled with γ' [Ni_3TiAl], γ" [Ni_3Nb], and δ [Ni_3Nb] phases/precipitates) in comparison with those parts produced by standard manufacturing methods [9, 10]. Nevertheless, it is said that the mechanical properties of the LPBF-built IN 718 alloy parts are better than those in conventional manufacturing [9–12]. It should also be noted that the LPBF-built nickel-based alloy components were not fully adopted by the aerospace and nuclear industry. This is because the parts of Inconel alloys fabricated by LPBF suffer from a relatively rough and uneven surface [13], surface defects [14], and columnar grains of anisotropic structure [15, 16], as well as excessive residual porosity [13] and tensile residual stresses [17] in the near-surface layers. The presence of excessive surface roughness with open pores, partially melted powder particles, and spattering powder particles can result in negative effects on both fatigue strength and corrosion resistance [18, 19].

The corrosion behavior of the nickel-based superalloy parts printed by the laser metal deposition [20, 21], the wire-arc metal deposition [22–24], the electron beam powder bed fusion [11, 25], and the laser beam powder bed fusion [26–28] techniques were recently observed and compared with conventional manufacturing methods [9, 11]. In particular, Klapper, et al. [26] confirmed that the build orientations do not result in an effect on the overall corrosion characteristics of the

LPBF-built IN 718 alloy parts in a highly corrosive environment containing 13 wt.% NaCl solution at 80°C. It was revealed that the LPBF-built IN 718 alloy parts contain a weak protective layer in a 3.5 wt.% NaCl solution [29]. Kong, et al. [8] reported that the corrosion rate for the LPBF-built Hastelloy X was larger than the wrought counterpart in aggressive environments due to the rapid dissolution of the places at the valleys and the molten pool boundaries, especially for the vertical section (XZ plane). Moreover, the passive film formed on the LPBF-built IN 718 alloy parts has a higher NiO content, resulting in the deterioration of its protective properties [30].

Therefore, the thermal [31–33], mechanical [14, 34, 35], chemical [20, 36], and combined thermo-mechanical [37, 38] or thermo-chemical [39] post-processing techniques should be applied to improve the physic-mechanical properties and reduce/eliminate the surface defects in the powder bed fused Ni-based alloys. To bring the LPBF-built Ni-based alloy components closer for critical/responsible applications becomes especially relevant. The hot isostatic pressing (HIP) [13, 15, 16] and heat post-treatments [15, 16, 40] are mainly applied to reduce subsurface porosity and change the dendritic structure to equal-grain structure while the mechanical/chemical surface post-treatments are used to improve residual stress state [34, 41, 42] and surface roughness [43, 44], as well as to reduce surface defects [17, 45, 46]. The study of corrosion behavior is crucial for the applications of the above-mentioned post-processing techniques, which lead to a variety of changes in structure and/or surface properties.

It should also be noted that the results showed that the corrosion resistance of the LPBF-built surfaces increased after mechanical surface treatment [9] and electropolishing [31, 47]. The LPBF-built IN 718 alloy parts treated by shot peening induced a stronger passive layer with higher magnitudes of pitting potential in comparison with the untreated sample [29]. This is because of a reduction of surface roughness from 12 to 2.5 μm [29] and the elimination of surface defects [48, 49]. Karthik, et al. [50] reported that compared to the untreated LPBF-printed specimen, the corrosion resistance of the LPBF-built IN 600 alloy parts was dramatically increased with a 10^6 fold decrease in corrosion rate after laser shock peening. Also, the stress corrosion resistance of the LPBF-built AlSi10Mg alloy samples was reduced by a mono-pin ultrasonic impact treatment [51]. This can be attributed to an increasing strain hardening due to the increase in the surface hardness, grain refinement, and material density in the near-surface layers [14, 52]. Additionally, the ultrasonic impact peening technique reduces the surface roughness and generates beneficial compressive residual stresses in additive-manufactured Inconel alloys [53]. It is well-known that the cracking can be significantly suppressed in the material deposited on the substrate by the ultrasonic impact treatment [54, 55]. Sun, et al. [56] showed that the cracks almost completely disappeared in the direct energy deposited of Inconel 100 superalloy at a higher impact load/energy. At the same time, the study of corrosion behavior in the LPBF-built IN 718 alloy post-processed by a barrel finishing, ultrasonic shot peening, and multi-pin ultrasonic impact treatment is virtually absent.

This work focuses on the correlation of the surface morphology, residual porosity, structure-phase state, microhardness, and chemical composition formed in the near-surface layers of Inconel 718 alloy by the laser powder bed fusion

Table 1 Nominal chemical composition of IN 718 powder (in weight percent, wt.%)

Ni	Cr	Fe	Nb	Mo	Ti	Al	C	Mn	Si
50–55	17–21	18–19.5	4.7–5.5	2.8–3.3	0.6–1.2	0.2–0.8	≤0.08	≤0.35	≤0.35
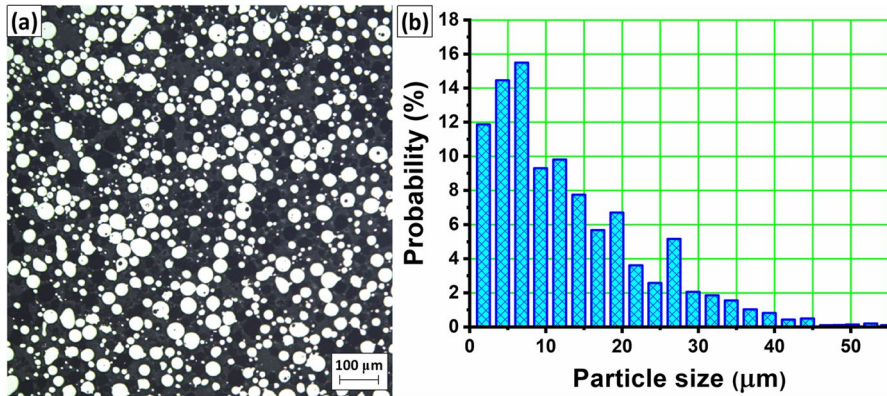
Fig. 1 Optical image (**a**) and particle size distribution (**b**) of the used IN 718 powder

fabrication and four optimized mechanical surface post-processing methods, i.e. barrel finishing, shot peening, ultrasonic shot peening, and multi-pin ultrasonic impact treatment, on the one hand, and the corrosion behavior of these surfaces in saline solution, on the other hand.

Material and Methods

Laser 3D printing details

Powder and specimens dimensions

A nickel-based pre-alloyed IN 718 powder was argon gas atomized and had a nominal chemical composition from the manufacturer as listed in Table 1. The used powder had a predominantly spherical shape (Fig. 1a), and its particle size distribution is shown in Fig. 1b [57]. It can be observed that almost all powder particles had a diameter < 50 μm with a volume median size of about 32.5 μm.

A test turbine blade IN 718 alloy part with base dimensions of 85.4 mm × 32.5 mm × 60 mm was fabricated in the Z direction using an LPBF machine [14]. After that, the turbine blade part was cut into three Sects. (85.4 mm × 32.5 mm × 20 mm) followed by further cut into plane specimen sizes

approximately 20 mm×20 mm×3.5 mm using an electrical discharge machining (EDM).

Laser powder bed fusion process

The test turbine blade parts were manufactured in an argon atmosphere using a laser powder bed fusion (LPBF) system (RENISHAW AM400 machine, United Kingdom), which consisted of scanning optics with a maximum scanning speed of 7000 mm/s and a maximum laser power of 400 W. An ytterbium fiber laser was used to melt the powder with a continuous laser mode at the laser power of 200 W. The powder layers of 60 μm were scanned with a scanning speed of 700 mm/s according to a multidirectional stripe scanning strategy, providing a focused laser spot size of 70 μm on the substrate and alternating by 67° between layers. The distance between stripes was 5 mm while the distance between lines was 90 μm. The used LPBF parameters were optimized for manufacturing nickel-based alloy parts [57, 58]. The LPBF-printed parts were removed from the building platform using EDM.

Mechanical surface post-processing techniques

The mechanical surface post-treatments, such as barrel finishing (BF), shot peening (SP), ultrasonic shot peening (USP), and ultrasonic impact treatment (UIT), were applied in the work to evaluate the progress on the effects of surface finishing/hardening on the surface properties and corrosion behavior of the Ni-based 718 alloy parts manufactured by the laser powder bed fusion technique. The above-mentioned mechanical surface post-treatments were applied under optimized parameters.

Barrel finishing

The wet BF treatment of the LPBF-built specimens was performed in a free state using equipment consisting of a six-sided barrel, media (steel shots), and compounds [52]. During this flexible and high-energy finishing method, the horizontal barrel was forcedly rotated in one direction by the motor with a rotation speed of 66 rpm, providing numerous high-speed collisions with very high pressures and considerable media sliding action within the barrel. The BF parameters used in the experiment were tailored to the surface treatment of the LPBF-built parts empirically. In this work, the BF process lasted for 4 h while the filling ratio of the barrel was 50%.

Shot peening

The SP treatment was manually applied on the LPBF-built superalloy specimens using industrial equipment at ambient temperature. The severe surface plastic deformation of the specimen was provided by bombardment with metal spherical shots of 0.5 mm diameter driven by the compressed air with a pressure of 0.55 MPa and a distance between the nozzle and the specimen surface of 30 mm. The used shots

were made of AISI 52100 bearing steel and an average hardness of 48 HRC. The specimens were high-intensity shot peened at optimized SP regimes for 2 min to achieve full surface coverage [52, 59].

Ultrasonic shot peening

The USP treatment was performed in a special chamber filled with a high-quality peening media (bearing balls with a diameter of 3.5 mm) [14]. An ultrasonic generator with a power output of 0.8 kW and a frequency of 21.6 kHz supplies a sinusoidal electric signal that induces a piezo-electric transducer to convert this electric energy into a mechanical displacement. The mechanical ultrasonic vibrations are amplified by the step-like ultrasonic horn to increase the kinetic energy, providing the amplitude of the ultrasonic horn of 40 μm. The horn tip vibration energy is directly in contact with the peening media, which acquired kinetic energy-produced severe plastic deformation of the surface LPBF-built specimens. The USP treatment was implemented at ambient temperature and treatment duration of 10 min using a distance between the surface specimen and the horn tip surface of 40 mm.

Ultrasonic impact treatment

The multi-pin UIT treatment is an advanced surface finishing and hardening technique, in which ultrasonic energy is produced by an electro-mechanical ultrasonic transducer, providing controllable surface treatment via the contact of specially designed steel pins. The used UIT system consisted of an ultrasonic generator with a power output of 0.8 kW and a frequency of 21.6 kHz, an ultrasonic vibration system with a piezoceramic transducer, a step-like horn, and a special multi-pin impact head with cylindrical pins of 5 mm diameter [14, 60]. The seven-pin impact head positioned on the horn tip was forcedly rotated during the treatment with a rotation speed of 76 rpm, providing high-frequency impacts of 1 ± 0.5 kHz. The LPBF-built superalloy specimens were treated by optimized UIT regimes (the amplitude of the ultrasonic horn was 18 μm, the treatment duration was 120 s, and the static load of the ultrasonic vibration system was 50 N) [61].

Specimen characterization

Surface morphology and roughness measurements

The surface quality in the vertical section of the LPBF-built and post-processed specimens was estimated with a 3D Taylor Hobson Form Talysurf 120 contact tester. The 3D surface morphology was analyzed in 3.0 mm by 3.0 mm area according to ISO 25178 standard. Additionally, the surface texture was analyzed by a Mitutoyo Hyper Quick Vision WLI 3D high-precision measuring system.

In this work, the 2D surface roughness profiles of the specimens were derived from 3D surface texture measurements and were expressed by the parameters of the arithmetical mean height (*Ra*), the maximum profile peak height (*Rp*) and profile valley depth (*Rv*), and the total height (*Rt*) of the profile along the sampling length for a roughness profile (ISO 4287 standard). Five measurements were done at different locations in the X-axis for each studied sample. The scatter of the experimental data was not exceeded by 5%. Average characteristics (skewness (asymmetry) and kurtosis (flatness) parameters) in the height direction of the roughness profiles were also studied [62–64].

Generally, the skewness *Rsk* and kurtosis *Rku* parameters coupled with the *Ssk* and *Sku* parameters obtained from the 3D surface texture were under special attention as possible key factors in the correlation between surface roughness/texture and the corrosion behavior because the skewness and kurtosis parameters are good indicators to predict the corrosion behavior [56].

Residual porosity and pore shape

The residual porosity was observed by a Leica MEF4A optical microscope equipped with a digital camera and a TESCAN Mira 3 LMU scanning electron microscope (SEM). To identify the residual pores, the studied specimens were mechanically cut into vertical (section perpendicular to the deposited layers – built section) cross-sections, ground, and polished according to a standard metallographic procedure. Firstly, the porosity was studied in the specimens without etching. Then, the specimens were electrolytically etched at 1–2 V dc by a Lucas' reagent consisting of lactic acid (50 ml), hydrochloric acid (150 ml), and oxalic acid (3 g) for 5 s.

The residual porosity of the LPBF-built and post-processed specimens was statistically analyzed in the specimens without etching using the Image-Pro Plus software. The sub-surface layers of about 0.5 mm thick were under analysis. Five fields in each specimen were analyzed to calculate the average area porosity *P* and standard deviation *S*. Additionally, several probabilistic parameters of the residual pores were determined to their precise characterization [65]. They are the following: the area *A* and average diameter *D* of spherical pores; the elongation *E* of the 'deformed' ('elliptic') pores, which is equal to the ratio of the minor (D_{min}) and major (D_{max}) axes of these 'deformed' pores; the major axis angle A_{MA}, which is the angle between specimen surface and the major axis of the 'deformed' pores.

Microstructure, microhardness and residual stress examinations

The microstructure and chemical composition in the vertical and horizontal cross-sections of the LPBF-built and mechanical surface post-processed specimens were observed by the high-resolution TESCAN Mira 3 LMU SEM microscope equipped with the energy-dispersive spectroscopy (EDS) detector OXFORD X-MAX 80 mm^2. As above-mentioned, the sectioned specimens were polished below 1 µm finish mechanically and cleaned ultrasonically in an acetone bath followed by electrolytic etching using a Lucas' reagent.

The near-surface microhardness profiles in the LPBF-fabricated and post-processed sample cross-sections (building direction) were measured from the surface (15–20 μm) towards the core material using a tester Leica VMHT with a Vickers indenter loaded by 0.025 kgf ($HV_{0.025}$) and the dwell time of 15 s. The standard deviation for the microhardness measurements was ± 1 HV.

The X-ray diffraction (XRD) analysis of the LPBF-built and post-processed (after the BF, SP, USP, and UIT) specimens were performed using a Rigaku Ultima IV diffractometer in a CuK_{α}-radiation with a graphite monochromator at 30 kV and 30 mA, a 2θ (20–120°) scanning speed of 2°/min. The phase compositions in the surface layers were determined using the XRD database. The residual macrostresses induced by the LPBF manufacturing and mechanical post-processing of the specimens' surface were also assessed using a standard sin2ψ based method.

Electrochemical measurements

All electrochemical corrosion measurements were carried out with the software-aided MTech PGP-550 M potentiostat/galvanostat connected to a classic three-electrode cell (electrolyte volume 0.5 L). Experiments were performed in a naturally aerated, near-neutral pH (7.7 $\pm$ 0.2) 3.5 wt.% NaCl, prepared with de-ionized water. The temperature of the test medium was equal in all experiments, i.e. $(21 \pm 0.5)^{\circ}$C. Each of the LPBF specimens in the initial and mechanically post-processed states was ultrasonically cleaned in ethanol and rinsed in de-ionized water and then placed in a Teflon holder. Then, the specimens were immediately positioned in the electrolytic cell and used as the working electrode. The area of the specimens exposed to the solution was ~ 0.4 cm^2. A saturated calomel electrode (SCE $= +244$ mV vs. SHE) and a platinum rod were respectively used as the reference and the counter electrodes [66]. All the potentials described in this work are relative to the SCE.

The following experiments were sequentially performed to evaluate the corrosion behavior of the LPBF-built specimens in the initial and mechanically post-processed states: (i) registering an evolution of open circuit potential with the holding time ($E_{ocp} = f(t)$), (ii) linear polarization resistance (LPR) measurements, and (iii) cyclic polarization (CP) [65, 67, 68].

Measurements of the open circuit potential E_{ocp} were performed for 10 min, and the attained potential was referred to as the corrosion potential E_{corr} at the end of the surface stabilization process. The linear polarization resistance (LPR) measurements, which involved disturbing the system with ± 30 mV vs. E_{corr}, were carried out after the stabilization of the studied surface. The potential scan rate was chosen to be 0.5 mV/s. The registered 'potential E vs. the current density i' data were then fitted by a straight line using the Origin Lab software. The values of the polarization resistance (R_p) were then determined as the slope of the 'E–i' curve ($R_p = (\Delta E / \Delta i)$).

The protective efficiency (P_{EF} [%]) of the mechanical surface treatment used was determined from LPR measurements by [65, 69]:

$$P_{EF} = \left[(R_{pol\_treated} - R_{pol\_LPBF})/R_{pol\_treated} \right] \bullet 100\%, \tag{1}$$

where R_{pol_LPBF} represents the polarization resistance of the LPBF-built surface, and $R_{pol\_treated}$ represents the polarization resistance of the surface of the mechanically post-processed specimens.

A cyclic polarization (CP) curves were registered in the anodic direction, starting at 250 mV more negative than E_{corr}. The CP tests were conducted at s scan rate of 0.5 mV/s. After achieving the switching potential E_{sw}, which was obtained at a pre-defined threshold current density ($i_{th}=2$ mA/cm^2), the polarization direction was reversed, and the backward scan curve was registered till its interception with the forward scan curve. The following essential potential parameters were obtained from the cyclic polarization curves. The corrosion potential (E_{corr}), corrosion current density (i_{corr}), and the cathodic/anodic Tafel slopes (b_c and b_a) were obtained by the intersection of the Tafel lines using computer-aided analysis. Additionally, when the current abruptly increases in the forward scan, the appropriate potential was registered to be the pitting potential (E_{pit}). The potential, which corresponds to the intersection of the backward scan and forward scan curves, was determined as the repassivation/protection potential (E_{rp}).

The corrosion rate (CR in mm year^{-1}) was calculated according to Faraday's law [70], in accordance with the ASTM G-59–97 standard [71]:

$$CR = 3.27 \cdot 10^{-3}(M/n) \cdot (1/\rho) \cdot i_{corr}, \tag{2}$$

where the factor $3.27 \bullet 10^{-3}$ contains the Faraday constant and the metric and time conversion factors, M is the molar mass, n is the valence, ρ is the density of the corroding metal and i_{corr} is the corrosion current density [μA cm^{-2}]. For Inconel 718, M/n ratio was determined by accounting for the concentrations and valences of all the elements, which compose the alloy and underwent the corrosion attack using the following formula [65]:

$$M/n = 1/ \sum (n_i \cdot f_i \cdot M_i), \tag{3}$$

where n_i is the valence of alloying element 'i', f_i is the mass fraction of alloying element 'i', and M_i is the molar mass of element 'i' (g/mole), whereas elements that have a mass fraction of more than 0.01 (more than 1% by weight) were included in the calculation.

Results and Discussion

Surface morphology and roughness

The surface texture of the studied parts in the LPBF-built state and after various mechanical surface post-treatments is presented in Fig. 2. Generally, the SP and UIT treatments led to a significant change in the surface morphology as compared to those of the BF and USP processed specimens. A completely new texture and no layer tracks on the surface were observed both for SP and UIT processed specimens (Figs. 3d, e). At the same time, the surface defects (spherical or ellipsoidal balls,
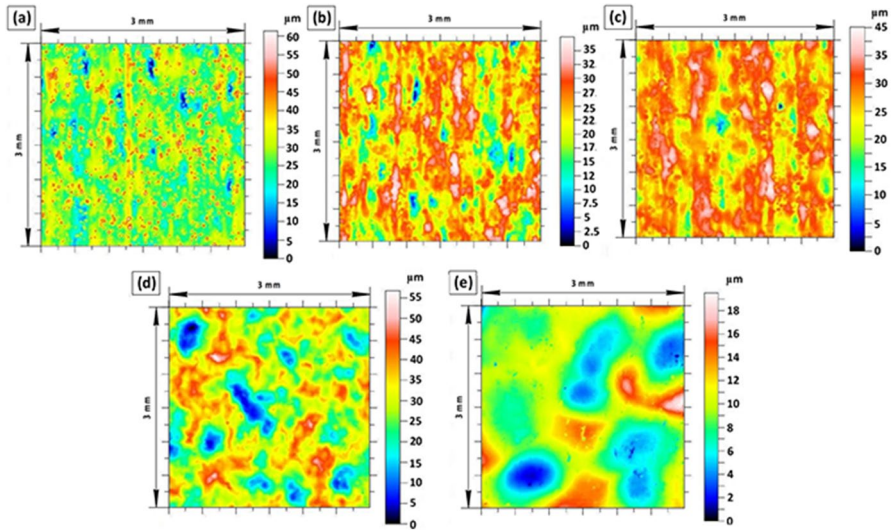
Fig. 2 Surface topography of the LPBF-built IN 718 alloy specimens in the initial state (**a**) and the BF (**b**), USP (**c**), SP (**d**), and UIT (**e**) post-processed specimens
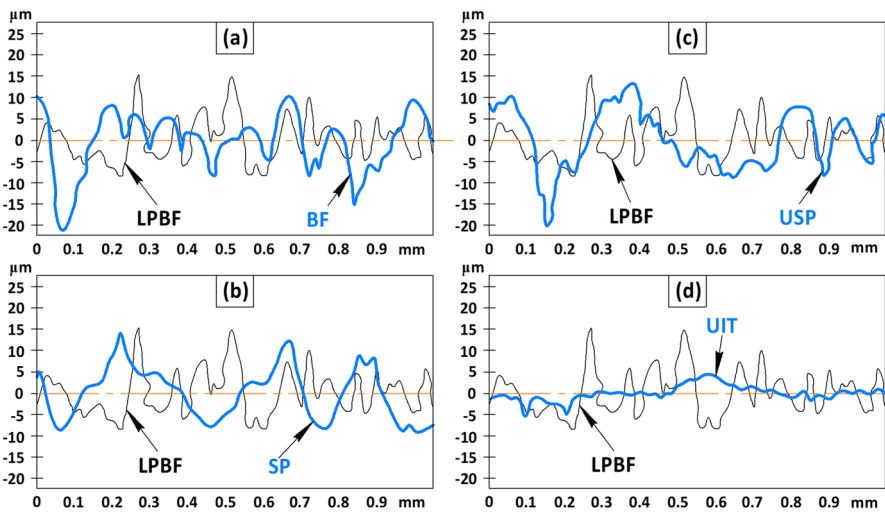

Fig. 3 Surface roughness profiles of the LPBF-built IN 718 alloy specimen after BF (**a**), SP (**b**), USP (**c**), and UIT (**d**) post-processing treatments

partially melted powder particles) were eliminated by all used mechanical surface treatments [14, 52].

The typical surface roughness profiles of the LPBF-built IN 718 alloy specimens after post-processing treatments are compared in Fig. 3. The total height of the roughness profile (Rt parameter) was reduced irrespective of the post-processing
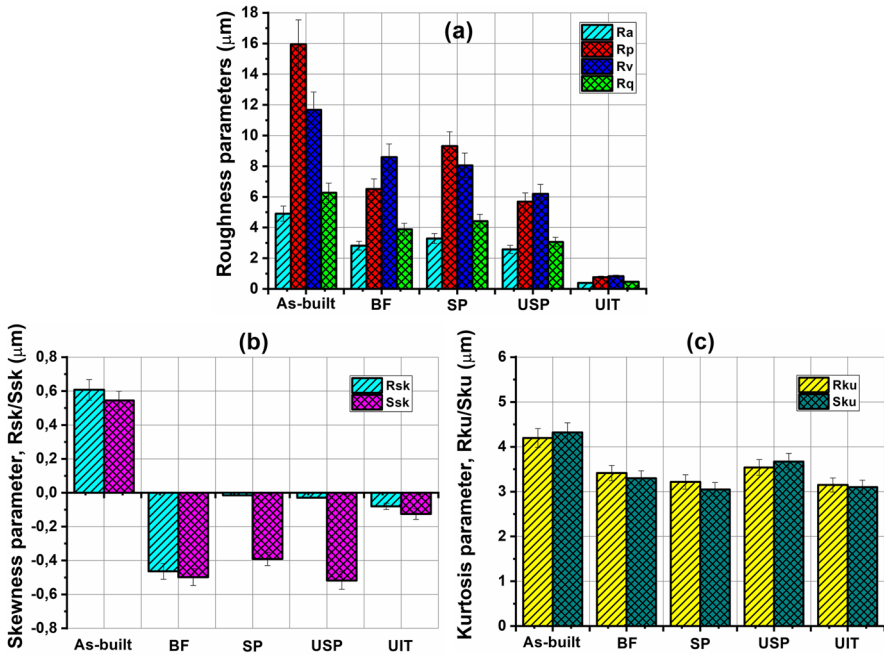
Fig. 4 Surface roughness parameters of the LPBF-built IN 718 alloy specimen after BF, SP, USP, and UIT post-processing treatments: **a** common amplitude parameters; **b** skewness; **c** kurtosis

used. It is clear that a surface roughness profile of the UIT-processed specimen (Fig. 3d) is characterized by a favorably smoother surface in comparison with those after the BF, SP, and USP treatments.

The LPBF-built specimens showed a rough surface roughness (*Ra* parameter) in a range of 4.08 – 5.60 μm due to the presence of various surface defects [59]. At the same time, increasing the surface roughness was shown to cause an increase in the corrosion rate [62] and thus should be minimized. Figure 4a shows the average surface roughness parameters of the untreated, barrel finished, shot peened, ultrasonic shot peened, and ultrasonic impact-treated LPBF-built specimens observed in this study. It can be seen that the UIT process produced the lowest surface roughness in the LPBF-built specimen with the average roughness *Ra* parameter of ~0.4 μm. Compared to the average surface roughness of the LPBF-built specimen (*Ra* ~ 5 μm), the *Ra* parameter was respectively decreased by 33.19%, 42.56%, and 47.45% after the SP, BF, and USP treatments.

The LPBF manufacturing process produces surfaces with positive skewness magnitudes, indicating the larger peak heights than valley depths for the roughness asperities (Fig. 5). It is well-known that the negative magnitudes of *Rsk* parameter point out that the surface consists of valleys, whereas the surface with a positive skewness is said to contain mainly peaks and asperities. It is also reported that a negatively skewed surface is beneficial for lubrication purposes while it conversely deteriorative as a factor activating/forming the corrosion pits [62].
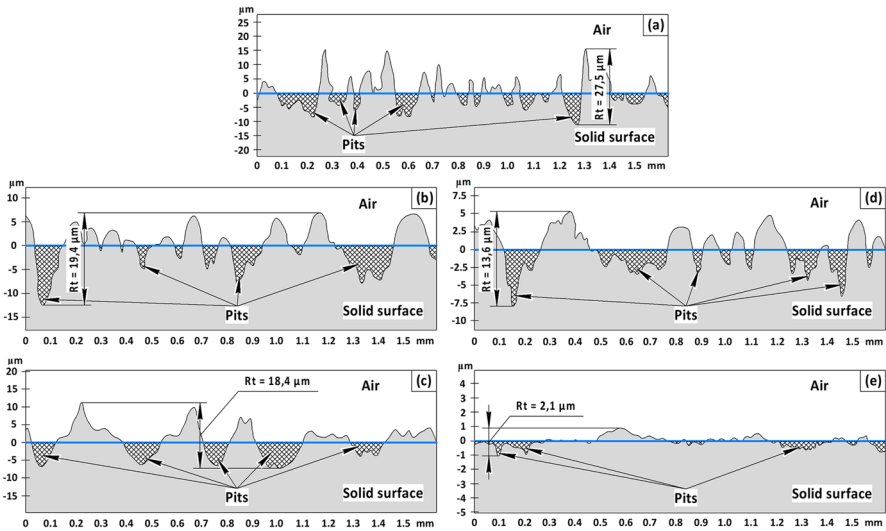
Fig. 5 Surface roughness profiles with evolution of pits in the LPBF-built IN 718 alloy specimens in the initial state (**a**) and the BF (**b**), SP (**c**), USP (**d**), and UIT (**e**) post-processed specimens

In our case, considering the skewness ($Rsk/Ssk \sim 0.6$ μm) and kurtosis ($Rku/Sku \sim 4.2$ μm is more than 3) values (Fig. 4b and 4c), the LPBF-built specimen may significantly suffer from the uniform and pitting corrosion. In contrast to the LPBF-built specimens, the application of the mechanical surface post-processing results in the negative skewness with magnitudes of Rku close to 3 (Fig. 4b and 4c). As a consequence, the skewness magnitudes are less than ± 2 and the reduction of the pitting/localized corrosion of the post-treated surfaces can be excepted although the uniform corrosion would be facilitated. Taking into account all these roughness factors (Figs. 4 and 5), the UIT-processed specimens present a higher corrosion resistance than those SP, USP, and BF-processed specimens. This is because new surface textures are created with a significantly smooth surface roughness profile ($Rt \sim 2$ μm), forming small-sized pits with a high degree of kurtosis ($Rku > 3$) (Fig. 5). The kurtosis magnitudes after the severe SP process are in good accordance with earlier works [72], where the kurtosis parameters were very close to 3. Our results are also in good correlation with the conclusions of J.M. Jaquez-Munoz et al. determined the corrosion mechanisms and corrosion kinetics of a number of titanium alloys based on the kurtosis and skewness magnitudes [73]. It was shown that uniform corrosion was operative at $Rsk < \pm 1$ and $Rku < 3$, pitting was observed at $Rsk > \pm 2$ and $Rku >> 3$, transgranular stress corrosion cracking (SCC) at $Rsk = -4$ and $Rku \sim 20$, and intergranular SCC at $Rsk = 1.5$–3.2 and $Rku = 6.4$–15.6.

Subsurface porosity

Production of pore- and defect-free surfaces and/or near-surface layers is known to be beneficial in improving the corrosion resistance because the porosity within the near-surface layer may accelerate local dissolution. Thus, porosity is considered the most important factor and should be minimized in order to enhance corrosion resistance. In this regard, it is of importance to analyze the effects of the used surface mechanical post-processing treatments on the average porosity of the LPBF-manufactured parts. To evaluate the porosity accurately, pores were analyzed in the selected fields of the same dimensions near the top surface of the specimen cross-sections.

Figure 6 shows the changes in the overall porosity (area porosity percentage) in the near-surface layer of ~350 μm thick of the LPBF-built specimens in the as-built state and after various post-processing treatments. The average porosity values are about three times higher in the building direction (BD) than those registered for the scanning direction (SD) of the LPBF-built specimens albeit the overall tendency to decrease after all mechanical post-processing is similar for both directions. The lowest average porosity values of ~0.032% and ~0.02% were respectively measured in the BD and SD directions after the UIT process. The efficiency of the used post-processing treatments can be arranged in the following ascending order: BF, SP, USP, and UIT, which correlates to the mechanical energy accumulated in the near-surface layers during the processes [14].

Thus, the decrease of porosity could originate from the severe plastic deformation that occurred during surface mechanical post-processing of the LPBF-built specimens. The strain-induced pores closure was earlier reported both for the powder
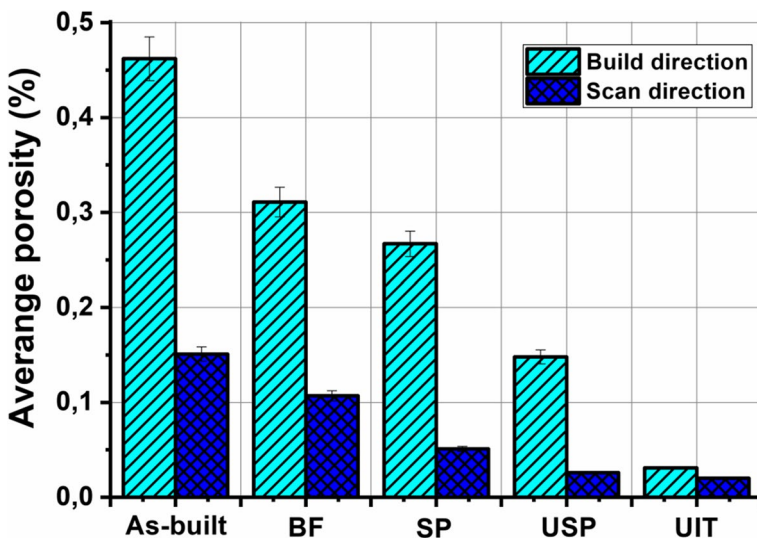

Fig. 6 Evolution of the pore area fraction in the surface layer of 350 μm thick of the LPBF-built IN 718 alloy specimen after BF, SP, USP, and UIT post-processing treatments

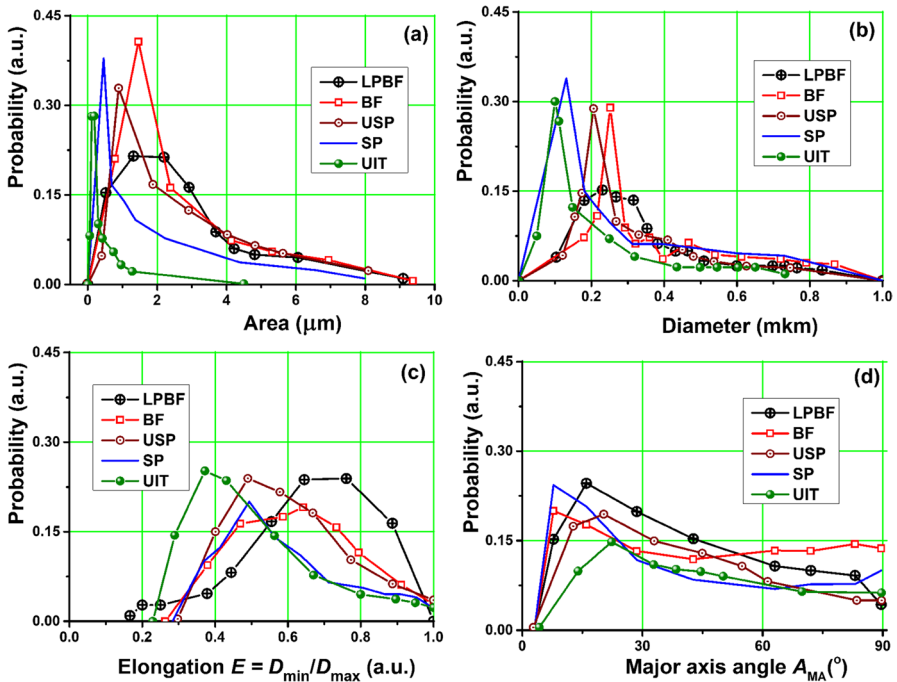**Fig. 7** Changes in the area fraction A (**a**), diameter D (**b**), shape (elongatopn E) (**c**) and major axis angle A_{MA} (**d**) of residual pores in the surface layer of the LPBF-built IN 718 alloy specimen after BF, SP, USP, and UIT post-processing treatments

Table 2 Characteristics of residual porosity and the pore shape in the surface layer of the LPBF-built and post-processed specimens of Inconel 718 alloy

Specimen	V_f (%)	V_f (%)	Most probable values from Fig. 7			
	BD*	SD*	A (μm)	D (μm)	A_{MA} (°)	$E = D_{min}/D_{max}$
LPBF	0.46	0.15	1.0–2.875	0.182–0.314	12–28	0.6–0.8
LPBF + BF	0.31	0.11	1.473	0.253	8–17	0.48–0.75
LPBF + USP	0.27	0.05	0.891	0.206	6–12	0.49–0.58
LPBF + SP	0.15	0.03	0.462	0.130	13–20	0.45–0.55
LPBF + UIT	0.032	0.02	0.119	0.099	21–23	0.35–0.45

* Abbreviations 'BD' and 'SD' are the built (ZX-plane) and scan (XY-plane) directions, respectively

metallurgy materials [74, 75], coatings [76], and selective laser melted IN 718 [14] specimens. Moreover, it was also suggested that these almost closed pores could be more prone to further healing during subsequent heat treatment than the spherical pores observed in the untreated as-built specimens [59]. Naturally, the decrease in the pore fracture in the top near-surface layer would diminish the quantity of micro-galvanic elements and thus retard the pitting development.

Figure 7 demonstrates the distributions of four parameters characterizing the individual pores located in the analyzed area, namely: the pore area A, pore diameter D, elongation E distribution, and major axis A_{MA} orientation regarding the specimen surface. The ImageProPlus software allows to measure and to analyze the objects on the binary image. Table 2 shows the most probable values of these distribution curves. Comparison of each of these parameters is important for the following reasons. The distributions of the pore area (Fig. 7a) and diameter (Fig. 7b) allow predicting the probable stress concentration on them and the ovelall operation life of the post-processed specimen/product. In our case, all mechanical post-processing treatments are seen to facilitate the decrease in the pore size and the increase in the probability of the pores of lower area (lower diameter) in comparison with the LPBF-built specimen. It means that more quantity of the pores of lower size would promote a more uniform distribution of internal stresses of any origin and would prevent possible stress concentration, cracks' initiation, and stress corrosion cracking.

The elongation E (Fig. 7c), which is the ratio between the minor D_{min} and major D_{max} axis lengths. ($E = D_{min}/D_{max}$), describes the pore shape. If the average or median elongation distribution is about 1, pores are more circular; if it is about 0, the pores are long and narrow. The right-skewed peak of the elongation distribution obtained for the LPBF-built specimen, which indicates the majority of circular pores, was transformed to the left-skewed distributions after mechanical post-processing treatments. It testifies about the increase in the number of horizontally oriented pores and/or pores of 'flattened' shape inclined to the surface due to deformation of the near-surface layer. These 'flattened' pores could be prone to further closure/healing at the subsequent heat treatment. However, narrow pores could be also more harmful concerning the possible formation of cracks and exfoliation.

Similar conclusions can be made by analyzing the major axis of a pore (Fig. 7d), which is a line that runs through the center of the pore between two edge points positioned at the longest distance. Angles between the surface and major axis are represented as absolute values between 0° and 90°. The angle between the surface and the major axis of a pore near 0° indicates a lamellar, horizontally oriented pore, and the angle of 90° points conversely to a normal orientation of the pore with regard to the specimen surface. In our case, the major axis-angle analysis reveals some left-skewed distributions both for the LPBF-built specimen and for mechanically post-processed ones. The major axis angles are observed to be distributed almost uniformly albeit a slight increase in the lower angles is evident. This indicates the presence and increment of lamellar porosity. This conclusion correlates well to the observed elongation distributions (Fig. 7c).

Residual stress and structure-phase state

The residual stress and structure-phase state affect fatigue strength and resistance of stress-corrosion cracking of the material. In this work, the X-ray macrostress analysis indicated the presentence of the tensile residual stresses formed in the LPBF-built IN 718 alloy parts (σ_R value is about $+120$ MPa) (Fig. 8).
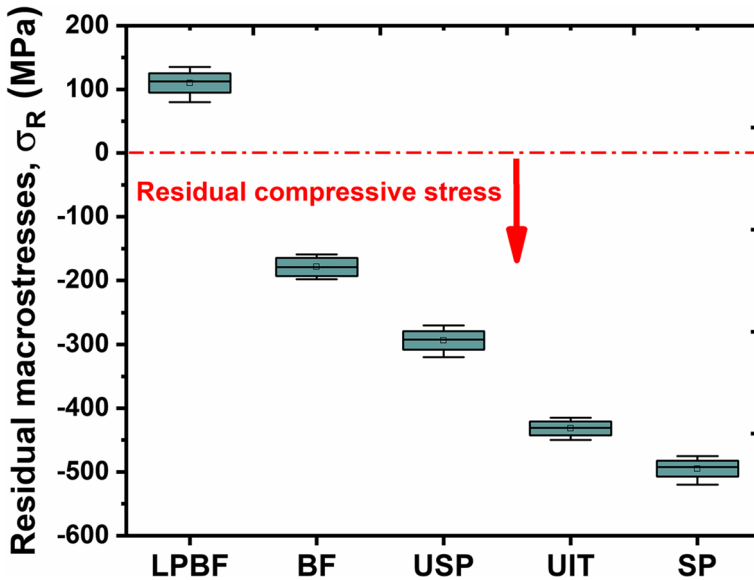
Fig. 8 Residual macrostress in the top surface layers of the LPBF-built and post-processed IN 718 alloy specimens

In contrast to the LPBF-built specimens, the severe plastic deformation induced by the mechanical treatments of the surface resulted in compressive residual macrostresses in the sub-surface layers, which are known to be beneficial in the sense of the anti-corrosion performance of a material. Accounting for the estimated magnitudes of compressive stresses formed in the top near-surface layer, the studied post-processing treatments can be positioned in the following ascending order: BF ($\sigma_R = -201.4$ MPa), USP ($\sigma_R = -313.8$ MPa), UIT ($\sigma_R = -428.7$ MPa), and SP ($\sigma_R = -510.7$ MPa) (Fig. 8). From point of view of desirable prolonged operation life of the LPBF-built parts, the higher the compressive stresses, the better operation life would be expected. The studied mechanical treatments resulted in severe plastic deformation of the treated surface. Therefore, the observed magnitudes of compressive residual stresses are in direct correlation with the induced strain extents, which naturally depends on the mechanical energy applied to the treated surface during these processes [14] and they can be adjusted by changing the process parameters (time and intensity) in accordance with the operational requirements.

Figure 9 illustrates the high-magnification images of the ZX cross-sections of the LPBF-built specimens (built direction) in the initial state and after various post-processing treatments. In comparison with the initial circular pores observed in the LPBF-built specimens (Fig. 9b), the shape of the residual pores was changed to become elongated due to the treatment-induced plastic deformation (Fig. 9c-f).

The chemical compositions of the dendrites and interdendritic areas in the initial LPBF-built (Fig. 9a) and UIT-processed (most deformed) (Fig. 9e) specimens are presented in Table 3. According to the EDX analysis (see the areas indicated
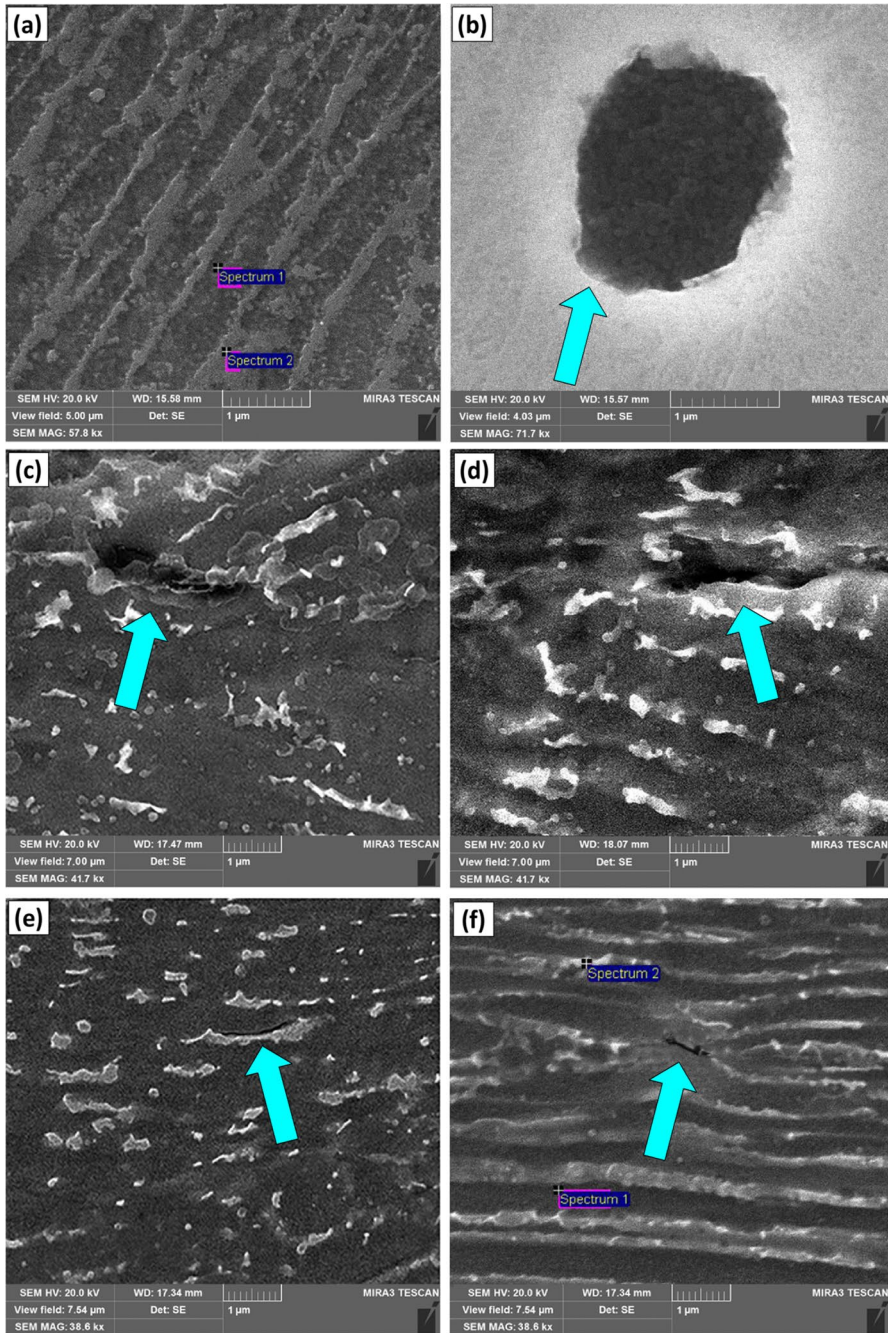
Fig. 9 SEM observations of the LPBF-built IN 718 alloy specimens in the initial state (**a**, **b**) and the BF (**c**), SP (**d**), USP (**e**) and UIT (**f**) post-processed specimens

Table 3 Energy dispersive data regarding chemical composition (in wt.%) of the LPBF-built specimens' surfaces before and after mechanical post-processing

Figure	Specimen	Spectrum	C	O	Al	Ti	Cr	Fe	Ni	Nb	Mo
Figure 9a	LPBF	# 1	2.17	0.38	0.51	0.92	16.21	16.91	53.65	6.03	3.22
	LPBF	# 2	2.91	0.41	0.38	0.99	16.43	16.38	52.54	6.78	3.18
Figure 9f	LPBF+UIT	# 1	2.60	0.35	0.34	0.81	16.67	17.16	53.20	5.94	2.93
	LPBF+UIT	# 2	3.08	0.37	0.44	0.89	16.61	17.10	51.83	6.44	3.24
-	LPBF	# 1	2.95	0.37	0.39	0.87	16.56	16.55	52.75	6.27	3.29
-	LPBF+BF	# 1	2.38	0.40	0.31	0.92	16.92	17.33	52.20	6.10	3.44
-	LPBF+USP	# 1	2.86	0.45	0.44	0.92	16.79	16.57	52.41	6.29	3.27
-	LPBF+SP	# 1	2.99	0.51	0.34	0.94	16.64	16.31	52.34	6.50	3.43
-	LPBF+UIT	# 1	2.96	0.54	0.38	0.83	16.75	16.48	52.38	6.45	3.23

in Fig. 9a, f and Table 3), the interdendritic areas are enriched with Nb, Ti, and C but depleted of Fe and Al. It can be the witness of the presence of carbides and γ'' (Ni_3Nb) phase in the interdendritic areas. The dendrites are conversely enriched with Ni, Fe, Mo, and Al indicating the presence of γ' ($Ni_3(AlTi)$ phase distributed in the γ solid solution (NiCrFeMo) [59, 77]. Another omportant conclusion regarding the corrosion behavior, which can be made, is that the phase compositions of the IN 718 alloy specimens can be considered almost unchanged after all mechanical surface post-treatments used.

The EDS analysis performed in the indicated areas was focused on seven elements of the alloy, i.e. nickel, chromium, iron, niobium, molibdenium, aluminium, and titanium. The accuracy of the EDS method allows obtaining an only rough estimation of the weight percentages of carbon and oxygen elements. The registered chemical compositions only insignificantly vary for the LPBF-built and post-processed specimens (Table 3). It relates both to dendrites and interdendritic areas (Fig. 9a, f) and to larger areas (450×450 μm^2) of the LPBF-built and post-processed surfaces. Therefore, this parameter can be considered to produce a similar effect on the corrosion behavior of the studied specimens. The observed chemical compositions will be used for the determination of the "molar mass – to – valence" (M/n) ratio of the alloy to assess the corrosion rate (see subsection 3.4).

It should also be noted that the applied mechanical surface treatments result in some diminishment in the cell/grain size and correspondingly increasing the surface hardness in the near-surface layers (Fig. 10). Taking into account the XRD data the crystallite size in the sub-surface layer is varied in a range of 10–35 nm after the used mechanical treatments. The UIT and SP processes provided the near-surface crystallite size is about 10–15 nm [59, 78].

The hardening depth in the LPBF-fabricated IN 718 alloy parts is varied in a range of 80–180 μm after the used mechanical surface post-processing. The hardening depth values are ~ 80 μm, ~ 140 μm, ~ 180 μm, and ~ 180 μm after BF, USP, SP, and UIT respectively. The BF and USP post-treatments lead to an
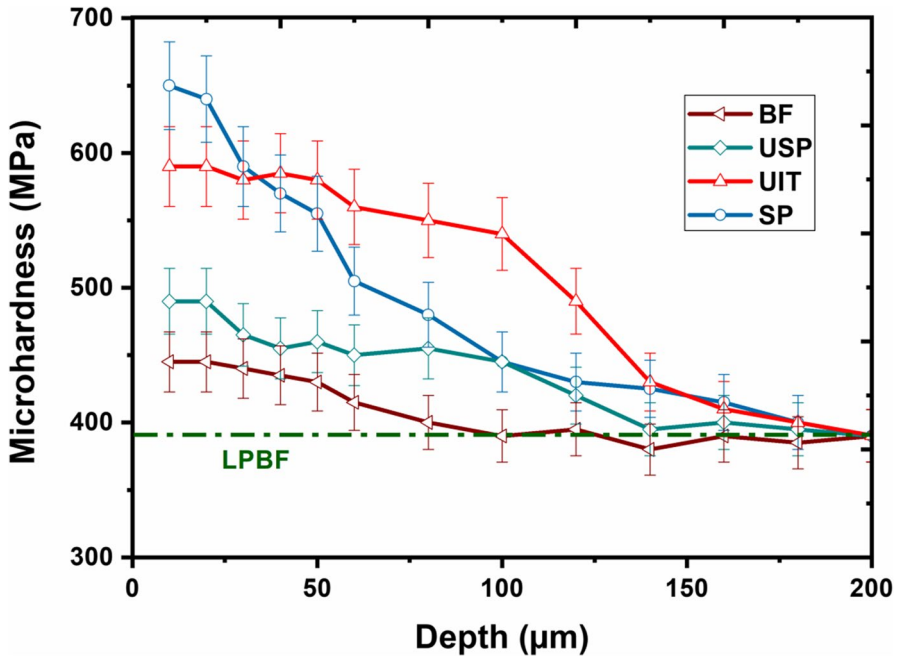
Fig. 10 Near-surface microhardness profiles along the building direction in the LPBF-built and post-processed IN 718 alloy specimens

increase in surface hardness by 15–20%, while the UIT and SP post-treatments results in an increase in hardness by 50–65%. These results confirm that the surfaces of the LPBF-fabricated IN 718 alloy parts were intensively deformed by the UIT / SP process. Notice, that similarly to the compressive residual stresses, the hardness magnitudes and hardening depths can be adjusted by changing the processing parameters, i.e., the applied mechanical energy [14]. This can be also applied to the corrosion-related data described below.

Corrosion

Open-circuit potential measurements

For the LPBF-built specimens in the initial state and after various mechanical post-processing treatments, the open circuit potential curves were registered during holding them in a 3.5 wt.% NaCl water solution for 600 s ($E_{OCP} = f[\tau]$) (Fig. 11). The registered E_{OCP} curves show that the as-built specimen exhibits the most negative value of open circuit potential and the BF-processed one demonstrates insignificantly changed E_{OCP} value. On the contrary, USP, SP, and UIT, which were performed at a higher intensity, resulted in the shift of the E_{ocp} curves toward the anodic direction, and the E_{OCP} magnitudes became less negative by 37 mV, 107 mV, and 115 mV, respectively. All studied specimens demonstrate slow descending overall trends,
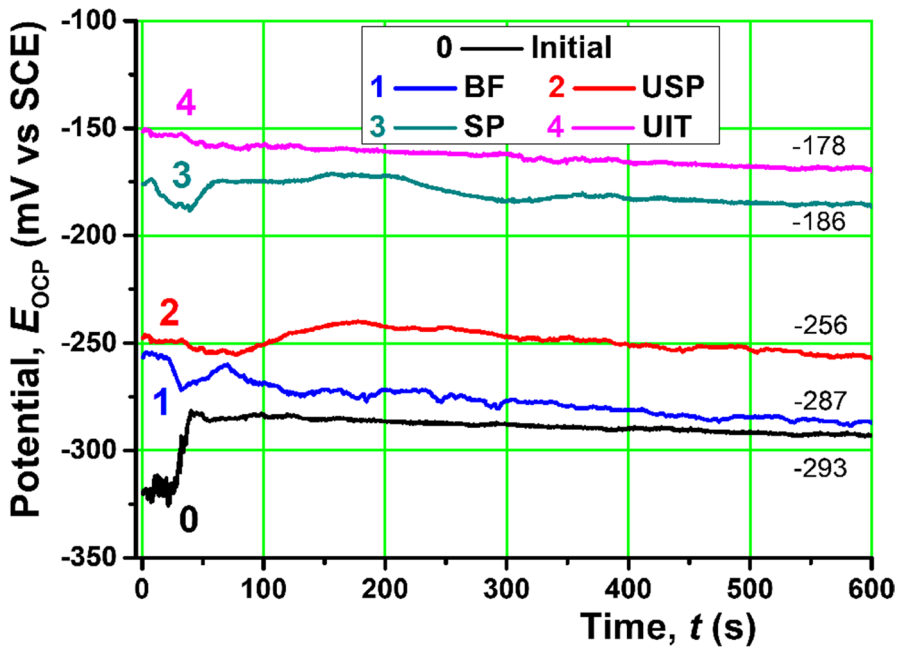
Fig. 11 Time dependencies of the open circuit potential E_{OCP} of the LPBF-built IN 718 alloy specimens in a 3.5 wt.% NaCl water solution (at $22 \pm 0.5°C$, pH 7.7 ± 0.2) before and after various mechanical post-processing treatments

indicating some dissolution of the specimen surface. Furthermore, the potentials of the initial and BF processed specimens demonstrate the quickest E_{OCP} decrease with the immersion time, which is naturally due to higher concentrations of the surface defects and porosity. The presence of unmolten surface particles, pores (including the interconnected pores), and cracks in the top near-surface layer may accelerate the formation of a galvanic couple leading to a fast dissolution in anodic places. Considering the E_{OCP} magnitudes registered at the end of open-circuit potential measurements, the corrosion resistance of the initial and post-processed LPBF-built specimens is expected to increase in the following order: LPBF < BF < USP < SP < UIT.

A good correlation between the surface roughness and average porosity data is also observed from the open circuit potential results. The lower corrosion resistance of the LPBF-built, BF, and USP processed specimens seems to be attributed to the higher content of defects on the outmost surface and pores in the top near-surface layer that has a crucial effect leading to corrosion. Both these features may also affect the integrity of the passivation films formed during polarization, which would determine the value of the polarization resistance (R_p). The R_p values can be assessed based on the registered linear polarization resistance (LPR) curves, which wil be analyzed in the next subsection.
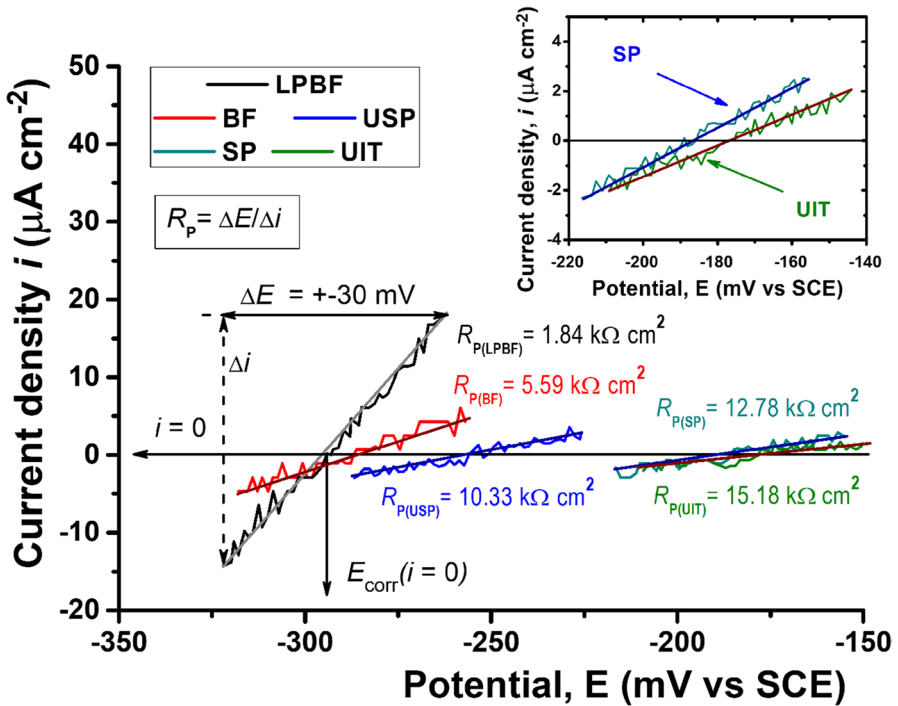
Fig. 12 Linear polarization resistance curves registered in a 3.5 wt.% NaCl solution in the potential interval of ± 30 mV vs E_{corr} of the LPBF-built and post-processed IN 718 alloy specimens

Linear polarization resistance measurements

Figure 12 compares the linear polarization resistance curves in a 3.5 wt.% NaCl solution, i.e. the dependencies of the current density i on the potential changed within the interval ± 30 mV around the corrosion potential E_{corr} (related to the zero current, i. e. corrosion current). The slopes of the linear curves are known to be inversely proportional to the polarization resistance R_p that occurs at a given applied potential [65, 79]. Thus, the R_p values for the LPBF-built and mechanically post-processed specimens can be assessed and compared using Fig. 12 and Table 3.

It is seen that all post-processing treatments strongly increase the R_p value, which was assessed to be the lowest for the LPBF-built specimen (1.84 kΩ cm^2). The R_p values ascend in the following order: LPBF < BF (5.59 kΩ cm^2) < USP (10.33 kΩ cm^2) < SP (12.78 kΩ cm^2) < UIT (15.18 kΩ cm^2). It is seen that mechanical post-processing treatments of higher intensity (USP, SP, and UIT) lead to essential R_p increase (literary by 5.6, ~ 7.0, and 8.2 times, respectively), viz. a higher resistance to uniform corrosion. Notice that the R_p increase order well correlates to that observed at the open-circuit potential measurements. The R_p magnitudes are convenient to perform the assessment of the protection efficiency of the modified surface using Eq. (1). Table 3 contains these P_{EF} values and shows that all studied
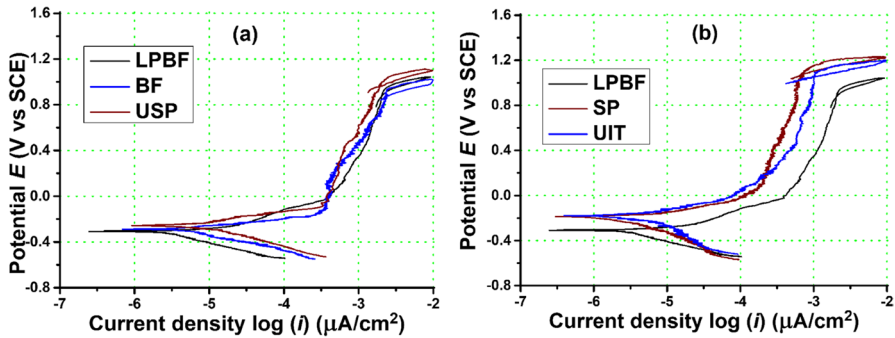
Fig. 13 Cyclic polarization curves measured in 3.5 wt.% NaCl water solution of the LPBF-built and post-processed IN 718 alloy specimens. (The characteristic values of electrochemical parameters are presented in Table 4)

mechanical post-processing treatments have a good efficiency (67–88%) in the sense of the retardation of specimen surface dissolution.

Cyclic polarization curves

Normally, cyclic polarization (CP) curves are known to describe the active/passive behavior of a material. Thus, they can be sussessfully used to analyze localized forms of corrosion [65, 80]. Figure 13 shows the typical cyclic polarization curves registered for the post-processed surfaces in comparison with that of the surface of the LPBF-built specimen. Additionally, appropriate electrochemical characteristics of the studied surfaces describing various corrosion-related processes are listed in Table 4.

R_p is the polarization resistance; E_{corr} is the corrosion potential; P_{EF} is the protective efficiency evaluated using Eq. (1); E_{ps} is the passivation potential; E_{pit} is the pitting potential; E_{rp} is the repassivation potential; E_{sw} is the switching potential.
[a] Parameters derived from LPR measurements; [b] Parameters determined from the CP curves.

It is seen that the corrosion potentials E_{corr} observed for the LPBF-built, BF-processed, and USP-processed specimens are similar to be –307 mV, –296 mV, and –291 mV, respectively (Fig. 13a, Table 4). On the contrary, the SP and UIT processes lead to a marked shift of the CP curves toward the anodic direction (Fig. 13b) exhibiting the noblest E_{corr} potentials (–197 mV and –199 mV, respectively). All registered curves show typical passivation behavior: the forward (anodic) scan of the CP curves of the LPBF-built and post-processed specimens demonstrate the first stage of active dissolution followed by a pronounced passive plateau caused by partial passivation. The passivation current i_{ps} values of the LPBF-built, BF-processed and USP-processed specimens are almost similar (Fig. 13a) while the SP-processed and UIT-processed specimens exhibit lower i_{ps} values (~3.7 μA/cm^2) in comparison with the LPBF-built specimen (~3.3 μA/cm^2) (Fig. 13b). Considering the slopes of the CP curves on the passivation stage the passivation ability can be

Table 4 Polarization resistance and characteristic potentials of the LPBF-built and post-processed IN 718 alloy specimens registered/assessed from linear/cyclic polarization measurements in naturally aerated 3.5 wt.% NaCl

Specimen	Parameters derived from LPR measurements		
	R_p (kΩcm)	E_{corr} (mV vs SCE)	P_{EF} (%)
LPBF	1.84	–293	-
LPBF+BF	5.59	–287	67.08
LPBF+USP	10.33	–256	82.18
LPBF+SP	12.78	–186	85.6
LPBF+UIT	15.18	–178	87.88
Specimen	Parameters determined from the CP curves				
	E_{corr} (mV vs SCE)	E_{ps} (mV vs SCE)	E_{pit} (mV vs SCE)	E_{rp} (mV vs SCE)	E_{sw} (mV vs SCE)
LPBF	–307	–29	918	870	1,040
LPBF+BF	–296	–142	947	877	1,014
LPBF+USP	–261	–89	994	963	1,097
LPBF+SP	–197	–27	1,092	1,074	1,223
LPBF+UIT	–199	50	1,086	1,054	1,196

R_p is a polarization resistance; E_{corr} is a corrosion potential; P_{EF} is the protective efficiency evaluated using Eq. (1); E_{ps} is a passivation potential; E_{pit} is a pitting potential; E_{rp} is a repassivation potential; E_{sw} is a switching potential

concluded almost similar although the evaluated passivation potentials E_{ps} are different (Table 3).

Additionally, the following electrochemical characteristics were also evaluated by considering the registered CP curves: the pitting potential E_{pit} indicating a sharp increase in the corrosion current after the end of the passivation stage; the switching potential E_{sw}, after which the backward curve was started; and the repassivation potential E_{rp} representing an intersection of the reverse and forward scan curves. Thus, the CP curves give evidence of a moderate (USP, BF in Fig. 13a) and significant (UIT, SP in Fig. 13b) increase in pitting potential in comparison with that of the LPBF-built specimen (Table 3). Notice that the reverse scans of all specimens show positive hysteresis, which did intersect the forward anodic scans. Furthermore, the E_{sw} and E_{rp} potentials for the UIT- and SP-processed specimens are also nobler than those for the LPBF-built and BF- or USP-processed ones. This observation is believed to relate to both the lowered surface roughness (dominated prior to initiation of pitting corrosion, $E < E_{pit}$) and lowered porosity percentage (affected the repassivation ability at $E > E_{pit}$) (see subsections 3.1 and 3.2, respectively). The skewness Rsk (Fig. 4b) and kurtosis Rku (Fig. 4c) parameters characterizing the surface microrelief are also well correlate to those values reported for the pitting resistant surfaces in the literature [73].

Analyzing several differences of the potentials registered for the LPBF-manufactured specimens allows evaluating the effects of the used post-processing techniques on the corrosion performance of the studied surfaces more precisely. The following parameters are useful: the region of passivity ($E_{pit} − E_C$) and the potential

difference $(E_{rp} - E_C)$ can respectively characterize the pitting initiation rate and the ability for repassivation, while the potential differences $(E_{pit} - E_{rp})$ and $(E_{sw} - E_C)$ can respectively describe the sensitivity of a material to crevice corrosion and the rate of anodic dissolution of the surface [65, 81]. Figure 14 compares the relative magnitudes of the above parameters evaluated for variously post-processed LPBF-built specimens. Following the referred works [65, 81, 82], the larger the $(E_{pit} - E_C)$ magnitude is known to relate to the slower the pitting initiation rate and the larger the $(E_{rp} - E_C)$ magnitude reflects the faster repasivation. Additionally, the larger the $(E_{pit} - E_{rp})$ magnitude the lower the resistance to the crevice corrosion is, and the larger the $(E_{sw} - E_C)$ magnitude the lower the anodic dissolution is.

In our case, the pitting initiation rates characterized by $(E_{pit} - E_{corr})$ are slower for all mechanically post-processed specimens (Fig. 14a) as compared to that of LPBF-built one, and it was found to descend in the following order: LPBF > BF > USP > UIT > SP. Anodic dissolution characterized by $(E_{sw} - E_C)$ magnitudes (Fig. 14b) is also observed to be lower for all post-processed specimens except the BF treated one, and it decreased in the following order: BF > LPBF > USP > SP > UIT. Additionally, all post-processed specimens except the BF-treated one demonstrate the higher ability for repassivation described by $(E_{rp} - E_{corr})$ (Fig. 14c), and it was found to ascend in the following order: BF > LPBF > USP > UIT > SP. Finally, the resistance to crevice corrosion was also improved by UIT, USP, and SP processes, and the (the $(E_{pit} - E_{rp})$ becomes lower in comparison with that of LPBF-built specimen, while the BF-processed specimens
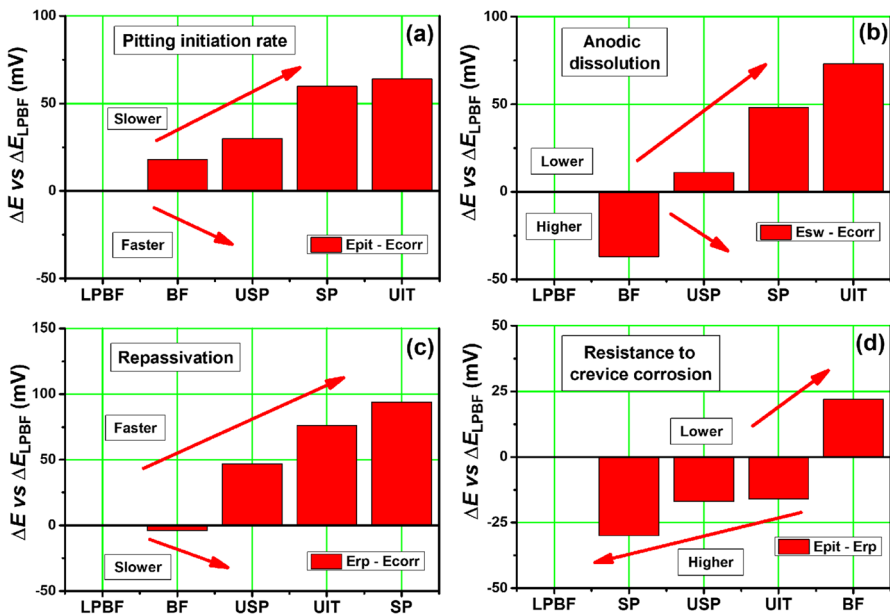

Fig. 14 Comparison of the trends of the evaluated potential differences ΔE obtained for the LPBF-built and post-processed IN 718 alloy specimens based on the linear/cyclic polarization measurements in naturally aerated 3.5 wt.% NaCl

became even worse than the LPBF-built one (Fig. 14d). Regarding the resistance of the specimens to crevice corrosion, the following descending order can be drawn: SP > USP > UIT > LPBF > BF. This observation correlates well to the EDX data indicating the appearance of some content of iron cladded during the BF process (see Table 3).

Corrosion rate

To make a quantitative comparison of the investigated specimens under steady-state conditions the corrosion rate values were determined. For this purpose, the ratio M/n was calculated using Eq. (3) by taking the registered chemical compositions of the studied surfaces (Table 5) and the density of the IN 718 alloy (being 8.34 g·cm^{-3}) into account. Only main metallic elements, i.e. nickel, chromium, iron, niobium, and molybdenium, which contents were higher than 1 wt.%, were used in the calculations.

The ratio of the molar mass to valence M/n was calculated to be of 13.826 g and the corrosion rate (in µm/year) for the IN 718 alloy specimen can thus be evaluated using the following formula:

$$CR = 5.42 \cdot i_{corr} \tag{4}$$

For all tested specimens, the corrosion current density (i_{corr}) was calculated as follows:

$$i_{corr} = b_a \cdot b_c / (2.303 \cdot R_p \cdot (b_a \cdot b_c)), \tag{5}$$

where R_p [kW cm^2] is the specific polarization resistance (determined from the linear polarization test) and ba and bc are the anodic and cathodic Tafel constants (in mV dec^{-1}) determined with the Tafel extrapolation method.

Magnitudes of the corrosion rate (CR), corrosion current density (i_{corr}), and anodic and cathodic Tafel constants are listed in Table 5. The post-processing treatments are seen to significantly influence the corrosion current density i_{corr} of the LPBF-built specimen (8.46 µA/cm^2). The lowest corrosion current densities i_{corr} of the UIT-processed and SP-processed specimens were calculated to be 1.01 µA/cm^2 and 1.21 µA/cm^2, respectively. Slightly higher i_{corr} values were registered for the specimens after two other post-processing treatments (USP and BF) to be 2.75 µA/cm^2 and 2.96 µA/cm^2,

Table 5 Tafel constants, corrosion current derived from electrochemical measurements for evaluation of the corrosion rate of the LPBF-built and post-processed IN 718 specimens in naturally aerated 3.5 wt.% NaCl

Specimen	b_a (mV/dec)	b_c (mV/dec)	i_{corr} (µA/cm^2)	CR (µm/year)
	Tafel extrapolation method		Equation (5)	Faraday's law Eq. (4)
LPBF	47	151	8.46	45.85
LPBF+BF	56	119	2.96	16.04
LPBF+USP	105	173	2.75	14.91
LPBF+SP	44	189	1.21	6.56
LPBF+UIT	56	96	1.01	5.47

respectively. Furthermore, the calculated values of corrosion rate were found to manifest a descend trend in the following sequence: LPBF > BF > USP > SP > UIT. Again, the UIT-processed and SP-processed specimens demonstrate the lowest corrosion rates (6.56 and 5.47 µm/year, respectively) and it is almost seven times lower compared to the LPBF-built specimen (45.85 µm/year).

Conclusions

The BF, SP, USP, and UIT mechanical surface treatments were applied to improve the IN 718 alloy parts fabricated by the LPBF additive manufacturing process. The effects of the mechanical post-processing treatments on the surface topography, porosity, residual stresses, sub-surface grain size and structure-phase state were studied. The obtained results allow drawing the following conclusions:

- The mechanical post-processing treatments are efficient methods for the diminishment of the surface roughness and elimination of the surface defects and porosity network, which in turn improves the anti-corrosion properties of the surface of the LPBF-built specimens. The flattened pores by severe plastic deformation may be prone to further closure/healing at the subsequent heat treatment of superalloy;
- The XRD study of surface microstructure revealed that the post-processing treatments formed the compressive residual stresses in the top near-surface layers of the LPBF-built specimens, which are beneficial in the improvement of the anti-corrosion properties. The magnitudes of compressive residual stresses formed in the top near-surface layer can be positioned in the following ascending order: BF (-201.4 MPa), USP (-313.8 MPa), UIT (-428.7 MPa), and SP (-510.7 MPa). SEM and EDS analysis reveal some structure refinement and insignificant changes in the chemical composition of the modified surfaces. The near-surface surface microhardness values were respectively achieved ~ 450, ~ 480, ~ 590, and ~ 650 $HV_{0.025}$ after BF, USP, UIT, and SP;
- Open circuit potential measurements show a gradual shift of the stable potentials of the studied surfaces after mechanical post-processing treatments toward anodic direction. The stable potential values and thus the corrosion resistance of the initial and post-processed LPBF-built specimens are expected to increase in the following order: LPBF < BF < USP < SP < UIT. A significant decrease in the average porosity is beneficial in decelerating the surface dissolution;
- Linear polarization resistance results allowed to assess the polarization resistance (R_p) values, which were observed to increase in the following order: LPBF (1.84 kΩ cm^2) < BF (5.59 kΩ cm^2) < USP (10.33 kΩ cm^2) < SP (12.78 kΩ cm^2) < UIT (15.18 kΩ cm^2). Protection efficiency P_{EF} values show that all studied mechanical post-processing treatments can be used to retard the specimen surface dissolution. There is a descending sequence of P_{EF} values: BF (67.1%), USP (82.2%), SP (85.6%), and UIT (87.9%);
- Cyclic polarizations curves confirmed that mechanical post-processing treatments can improve the LPBF-built specimens making them nobler with the lower

corrosion rate in the following descending order: LPBF (45.85 μm/year) < BF (16.04 μm/year) < USP (14.91 μm/year) < SP (6.56 μm/year) < UIT (5.47 μm/year). The UIT and SP treatments provided the highest reduction in the corrosion rate, which almost achieved the factor of more than 8 and ~ 7, respectively;

- The pitting initiation rates were found to be in the descending order: LPBF > BF > USP > UIT > SP. Anodic dissolution decreased in the following order: BF > LPBF > USP > SP > UIT. Ability for repassivation was found to ascend as follows: BF > LPBF > USP > UIT > SP. The resistance of the specimens to crevice corrosion can be drawn in the following order: SP > USP > UIT > LPBF > BF;

- The type and regime of appropriate mechanical surface post-processing technique can be selected based on the time/energy consuming, the surface quality requirements, and shape/dimensions of the LPBF-fabricated IN 718 alloy parts to be processed. The multi-pin UIT treatment can be applied for the surface finishing and hardening of large LPBF-printed parts while the USP technique for the surface treatment of small and complexly shaped LPBF-printed parts. The SP process is effective for the surface treatment of both large and small LPBF-printed parts, including the complexly shaped parts. The BF treatment can be applied predominantly for surface finishing, but after sandblasting/shot peening.

Data Availability The dataset generated and analyzed during the current study are available from the corresponding author on reasonable request.

Declarations

Ethical Approval No ethical approval was required for this research.

Competing interests The authors declare no competing interests.

References

1. Osoba, L.O., Oladoye, A.M., Ogbonna, V.E.: Corrosion evaluation of superalloys Haynes and Inconel 718 in hydrochloric acid. J. Alloys Compd. **804**, 376–384 (2019). https://doi.org/10.1016/j.jallcom.2019.06.196

2. Frazier, W.E.: Metal additive manufacturing: A review. J. Mater. Eng. Perform. **23**, 1917–1928 (2014). https://doi.org/10.1007/s11665-014-0958-z

3. Wang, X., Gong, X., Chou, K.: Review on powder-bed laser additive manufacturing of Inconel 718 parts. Proc. of the Institution of Mechanical Engineers. Part B: J. Eng. Manuf. **231**, 1890–1903 (2017). https://doi.org/10.1177/0954405415619883

4. Karia, M.C., Popat, M.A., Sangani, K.B.: selective laser melting of inconel super alloy – A review. AIP Conference Proc. **1859**, 020013–020020 (2017). https://doi.org/10.1063/1.4990166

5. Witkin, D.B., Patel, D.N., Helvajian, H., Steffeney, L., Diaz, A.: Surface treatment of powder-bed fusion additive manufactured metals for improved fatigue life. J. Mater. Eng. Perform. **28**, 681–692 (2019). https://doi.org/10.1007/s11665-018-3732-9

6. Wang, Y., Shi, J., Lu, S., Wang, Y.: Selective laser melting of graphene-reinforced Inconel 718 superalloy: Evaluation of microstructure and tensile performance. Manuf. Sci. Eng. **139**, 8683–8691 (2017). https://doi.org/10.1115/1.4034712

7. Lesyk, D.A., Martinez, S., Dzhemelinskyi, V.V., Lamikiz, A.: Additive manufacturing of the super-alloy turbine blades by selective laser melting: Surface quality, microstructure and porosity, NT 2020. Lect. Notes Netw. Syst. **128**, 267–275 (2020). https://doi.org/10.1007/978-3-030-46817-0_30

8. Kong, D., Ni, X., Dong, C., Zhang, L., Yao, J., Man, C., Wanga, L., Xiao, K., Li, X.: Anisotropic response in mechanical and corrosion properties of hastelloy X fabricated by selective laser melting. Constr. Build. Mater. **221**, 720–729 (2019). https://doi.org/10.1016/j.conbuildmat.2019.06.132

9. Cabrini, M., Lorenzi, S., Testa, C., Pastore, T., Brevi, F., Biamino, S., Fino, P., Manfredi, D., Marchese, G., Calignano, F., Scenini, F.: Evaluation of corrosion resistance of alloy 625 obtained by laser powder bed fusion. J. Electrochem. Soc. **166**(11), C3399 (2019). https://doi.org/10.1149/2.0471911jes

10. Trosch, T., Strobner, J., Volkl, R., Glatzel, U.: Microstructure and mechanical properties of selective laser melted Inconel 718 compared to forging and casting. Mater. Lett. **164**, 428–431 (2016). https://doi.org/10.1016/j.matlet.2015.10.136

11. Basak, S., Sharma, S.K., Sahu, K.K., Gollapudi, S., Majumdar, J.D.: Surface modification of structural material for nuclear applications by electron beam melting: enhancement of microstructural and corrosion properties of Inconel 617. SN Appl. Sci. **1**(7), 708 (2019). https://doi.org/10.1007/s42452-019-0744-5

12. Wang, Z., Guana, K., Gaoa, M., Li, X., Chen, X., Zeng, X.: The microstructure and mechanical properties of deposited-IN718 by selective laser melting. J. Alloy. Compd. **513**, 518–523 (2012). https://doi.org/10.1016/j.jallcom.2011.10.107

13. Mostafa, A., Rubio, I.P., Brailovski, V., Jahazi, M., Medraj, M.: Structure, texture and phases in 3D printed IN718 alloy subjected to homogenization and HIP treatments. Metals. **7**, 196–219 (2017). https://doi.org/10.3390/met7060196

14. Lesyk, D.A., Martinez, S., Mordyuk, B.N., Dzhemelinskyi, V.V., Lamikiz, A., Prokopenko, G.I.: Post-processing of the Inconel 718 alloy parts fabricated by selective laser melting: Effects of mechanical surface treatments on surface topography, porosity, hardness and residual stress. Surf. Coat. Technol. **381**, 125136 (2020). https://doi.org/10.1016/j.surfcoat.2019.125136

15. Kuo, Y.L., Nagahari, T., Kakehi, K.: The effect of post-processes on the microstructure and creep properties of alloy718 built up by selective laser melting. Mater. **11**, 996–1009 (2018). https://doi.org/10.3390/ma11060996

16. Seede, R., Mostafa, A., Brailovski, V., Jahazi, M., Medraj, M.: Microstructural and microhardness evolution from homogenization and hot isostatic pressing on selective laser melted Inconel 718: Structure, texture, and phases. Manuf. Mater. Process. **2**, 30–51 (2018). https://doi.org/10.3390/jmmp2020030

17. Thiede, T., Cabeza, S., Mishurova, T., Kromm, A., Bode, J., Haberland, C., Bruno, G.: Residual stress in selective laser melted Inconel 718: Influence of the removal from base plate and deposition hatch length. Mater. Perform. Character. **7**, 0119–0138 (2017). https://doi.org/10.1520/MPC20170119

18. Sander, G., Tan, J., Balan, P., Gharbi, O., Feenstra, D.R., Singer, L., Thomas, S., Kelly, R.G., Scully, J.R., Birbilis, N.: Corrosion of additively manufactured alloys: A review. Corros. **74**(12), 1318–1350 (2018). https://doi.org/10.5006/2926

19. Dryepondt, S., Kirka, M.M., List III, F.A.: Oxidation behavior of Ni-based alloys fabricated by additive manufacturing. In: Paper presented at the CORROSION 2019, Nashville (2019) NACE-2019-13558. https://www.osti.gov/servlets/purl/1658013

20. Guo, P., Lina, X., Li, J., Zhang, Y., Song, M., Huang, W.: Electrochemical behavior of Inconel 718 fabricated by laser solid forming on different sections. Corros. Sci. **132**, 79–89 (2018). https://doi.org/10.1016/j.corsci.2017.12.021

21. Kong, D., Dong, C., Ni, X., Zhang, L., Man, C., Zhu, G., Yao, J., Yao, J., Wang, L., Cheng, X., Li, X.: Effect of TiC content on the mechanical and corrosion properties of Inconel 718 alloy fabricated by a high-throughput dual-feed laser metal deposition system. J. Alloys Compd. **803**, 637–648 (2019). https://doi.org/10.1016/j.jallcom.2019.06.317

22. Asala, G., Andersson, J., Ojo, O.A.: Hot corrosion behaviour of wire-arc additive manufactured Ni-based superalloy ATI 718Plus®. Corros. Sci. **158**, 108086 (2019). https://doi.org/10.1016/j.corsci.2019.07.010

23. Wang, Y., Chen, X.: Investigation on the microstructure and corrosion properties of Inconel 625 alloy fabricated by wire arc additive manufacturing. Mater. Res. Express. **6**(10), 106568 (2019). https://doi.org/10.1088/2053-1591/ab39f6

24. Zhang, L.N., Ojo, O.A.: Corrosion behavior of wire arc additive manufactured Inconel 718 superalloy. J. Alloys Compd. **829**, 154455 (2020). https://doi.org/10.1016/j.jallcom.2020.154455

25. Karimi, P., Sadeghi, E., Algardh, J., Harlin, P., Andersson, J.: Effect of build location on microstructural characteristics and corrosion behavior of EB-PBF built alloy 718. Int. J. Adv. Manuf. Technol. **106**(7), 3597–3607 (2020). https://doi.org/10.1007/s00170-019-04859-9

26. Klapper, H.S., Molodtsov, N., Burns, M., Wangenheim, C.: Critical factors affecting the pitting corrosion resistance of additively manufactured nickel alloy in chloride containing environments, Corros. 2017, paper no. 9345. NACE, Houston TX (2017)

27. Lefky, C.S., Gallmeyer, T.G., Moorthy, S., Stebner, A., Hildreth, O.J.: Microstructure and corrosion properties of sensitized laser powder bed fusion printed Inconel 718 to dissolve support structures in a self-terminating manner. Addit. Manuf. **27**, 526–532 (2019). https://doi.org/10.1016/j.addma.2019.03.020

28. Kong, D., Dong, C., Ni, X., Li, X.: Corrosion of metallic materials fabricated by selective laser melting. NPJ Mater. Degrad. **3**, 24 (2019). https://doi.org/10.1038/s41529-019-0086-1

29. Mythreyi, O.V., Raja, A., Nagesha, B.K., Jayaganthan, R.: Corrosion study of selective laser melted IN718 alloy upon post heat treatment and shot peening. Metals. **10**(12), 1562 (2020). https://doi.org/10.3390/met10121562

30. Tang, Y., Shen, X., Qiao, Y., Yang, L., Chen, J., Lu, D., Zhang, Z.: Corrosion behavior of a selective laser melted Inconel 718 alloy in a 3.5 wt.% NaCl solution. J. Mater. Eng. Perform. **30**, 5506–5514 (2021). https://doi.org/10.1007/s11665-021-05909-8

31. Juillet, C., Oudriss, A., Balmain, J., Feaugas, X., Pedraza, F.: Characterization and oxidation resistance of additive manufactured and forged IN718 Ni-based superalloys. Corros. Sci. **142**, 266–276 (2018). https://doi.org/10.1016/j.corsci.2018.07.032

32. Li, H., Feng, S., Li, J., Gong, J.: Effect of heat treatment on the δ phase distribution and corrosion resistance of selective laser melting manufactured Inconel 718 superalloy. Corros. Mater. **69**(10), 1350–1354 (2018). https://doi.org/10.1002/maco.201810159

33. Lesyk, D.A., Martinez, S., Pedash, O.O., Dzhemelinskyi, V.V., Lamikiz, A.: Porosity and surface defects characterization of hot isostatically pressed Inconel 718 alloy turbine blades printed by 3D laser metal fusion technology. MRS Adv. **7**, 197–201 (2022). https://doi.org/10.1557/s43580-021-00187-x

34. Maleki, E., Unal, O., Guagliano, M., Bagherifard, S.: The effects of shot peening, laser shock peening and ultrasonic nanocrystal surface modification on the fatigue strength of Inconel 718. Mater. Sci. Eng. A. **810**, 141029 (2021). https://doi.org/10.1016/j.msea.2021.141029

35. Lee, S., Shao, S., Wells, D.N., Zetek, M., Kepka, M., Shamsaei, N.: Fatigue behavior and modeling of additively manufactured IN718: The effect of surface treatments and surface measurement techniques. J. Mater. Process. Technol. **302**, 117475 (2022). https://doi.org/10.1016/j.jmatprotec.2021.117475

36. Dehghanghadikolaei, A., Ibrahim, H., Amerinatanzi, A., Hashemi, M., Moghaddam, N.S., Elahinia, M.: Improving corrosion resistance of additively manufactured nickel–titanium biomedical devices

by microarc oxidation process. J. Mater. Sci. **54**(9), 7333–7355 (2019). https://doi.org/10.1007/s10853-019-03375-1

37. Lesyk, D.A., Martinez, S., Pedash, O.O., Mordyuk, B.N., Dzhemelinskyi, V.V., Lamikiz, A.: Nickel superalloy turbine blade parts printed by laser powder bed fusion: Thermo-mechanical post-processing for enhanced surface integrity and precipitation strengthening. J. Mater. Eng. Perform. **31**, 6283–6299 (2022). https://doi.org/10.1007/s11665-022-06710-x

38. Lesyk, D.A., Martinez, S., Mordyuk, B.N., Pedash, O.O., Dzhemelinskyi, V.V., Lamikiz, A.: Ultrasonic surface post-processing of hot isostatic pressed and heat treated superalloy parts manufactured by laser powder bed fusion. Addit. Manuf. Lett. **3**, 100063 (2022). https://doi.org/10.1016/j.addlet.2022.100063

39. Sadeghi, M., Diaz, A., McFadden, P., Sadeghi, E.: Chemical and mechanical post-processing of Alloy 718 built via electron beam-powder bed fusion: Surface texture and corrosion behavior. Mater. Des. **214**, 110405 (2022). https://doi.org/10.1016/j.matdes.2022.110405

40. Raghavan, S., Zhang, B., Wang, P., Sun, C.N., Nai, M.L.S., Li, T., Wei, J.: Effect of different heat treatments on the microstructure and mechanical properties in selective laser melted Inconel 718 alloy. Mater. Manuf. Process. **32**, 1588–1595 (2017). https://doi.org/10.1080/10426914.2016.1257805

41. Jinoop, A.N., Kanmani Subbu, S., Paul, C.P., Palani, I.A.: Post-processing of laser additive manufactured Inconel 718 using laser shock peening. Int. J. Precis. Eng. Manuf. **20**, 1621–1628 (2019). https://doi.org/10.1007/s12541-019-00147-4

42. Munther, M., Tajyar, A., Holtham, N., Hackel, L., Beheshti, A., Davami, K.: An investigation into the mechanistic origin of thermal stability in thermal-microstructural-engineered additively manufactured Inconel 718. Vacuum. **199**, 110971 (2022). https://doi.org/10.1007/s12541-019-00147-4

43. Kaynak, Y., Tascioglu, E.: Post-processing effects on the surface characteristics of Inconel 718 alloy fabricated by selective laser melting additive manufacturing. Prog. Addit. Manuf. **5**, 221–234 (2020). https://doi.org/10.1007/s40964-019-00099-1

44. Boschetto, A., Bottini, L., Macera, L., Veniali, F.: Post-processing of complex SLM parts by barrel finishing. Appl. Sci. **10**, 1382 (2020). https://doi.org/10.3390/app10041382

45. Balbaa, M., Ghasemi, A., Fereiduni, E., Al-Rubaie, K., Elbestawi, M.: Improvement of fatigue performance of laser powder bed fusion fabricated IN625 and IN718 superalloys via shot peening. J. Mater. Process. Technol. **304**, 117571 (2022). https://doi.org/10.1016/j.jmatprotec.2022.117571

46. Lesyk, D.A., Dzhemelinskyi, V.V., Martinez, S., Grzesiak, D., Mordyuk, B.N.: Functional evaluation of surface texture in laser selective melted Inconel 718 alloy parts processed by shot peening, InterPartner 2022. Lect. Notes Mech. Eng. (2023) 294. –305. https://doi.org/10.1007/978-3-031-16651-8_28

47. Zhang, B., Xiu, M., Tan, Y.T., Wei, J., Wang, P.: Pitting corrosion of SLM Inconel 718 sample under surface and heat treatments. Appl. Surf. Sci. **490**, 556–567 (2019). https://doi.org/10.1016/j.apsusc.2019.06.043

48. Lesyk, D.A., Martinez, S., Dzhemelinskyi, V.V., Stamann, O., Mordyuk, B.N., Lamikiz, A.: Surface polishing of laser powder bed fused superalloy components by magnetic post-treatment. NAP. **2020**, 02SAMA17-1–02SAMA17-4 (2020). https://doi.org/10.1109/NAP51477.2020.9309600

49. Lesyk, D.A., Martinez, S., Pedash, O.O., Dzhemelinskyi, V.V., Mordyuk, B.N.: Combined thermo-mechanical techniques for post-processing of the SLM-printed Ni-Cr-Fe alloy parts, DSMIE 2020. Lect. Notes Mech. Eng. 295–304 (2020). https://doi.org/10.1007/978-3-030-50794-7_29

50. Karthik, D., Swaroop, S.: Laser shock peening enhanced corrosion properties in a nickel based Inconel 600 superalloy. J. Alloy. Compd. **694**, 1309–1319 (2017). https://doi.org/10.1016/j.jallcom.2016.10.093

51. Xing, X., Duan, X., Jiang, T., Wang, J., Jiang, F.: Ultrasonic peening treatment used to improve stress corrosion resistance of AlSi10Mg components fabricated using selective laser melting. Metals. **9**, 103–111 (2019). https://doi.org/10.3390/met9010103

52. Lesyk, D.A., Martinez, S., Mordyuk, B.N., Dzhemelinskyi, V.V., Lamikiz, A.: Surface finishing of complexly shaped parts fabricated by selective laser melting, InterPartner-2019. Lect. Notes Mech. Eng. 186–195 (2020). https://doi.org/10.1007/978-3-030-40724-7_19

53. Jiménez, A., Bidare, P., Hassanin, H., Tarlochan, F., Dimov, S., Essa, K.: Powder-based laser hybrid additive manufacturing of metals: a review. Int. J. Adv. Manuf. Technol. **114**, 63–96 (2021). https://doi.org/10.1007/s00170-021-06855-4

54. Wang, Y., Shi, J.: Microstructure and properties of Inconel 718 fabricated by directed energy deposition with in-situ ultrasonic impact peening. Metall. Mater. Trans. B. **50**, 2815–2827 (2019). https://doi.org/10.1007/s11663-019-01672-3

55. Wang, Y., Shi, J.: Recrystallization behavior and tensile properties of laser metal deposited Inconel 718 upon in-situ ultrasonic impact peening and heat treatment. Mater. Sci. Eng. A. **786**, 139434 (2020). https://doi.org/10.1016/j.msea.2020.139434

56. Sun, L., Huang, L., Wu, P., Huang, R., Fang, N., Xu, F., Xu, K.: Progress on the effect and mechanism of ultrasonic impact treatment on additive manufactured metal fabrications. Metall. Mater. Trans. B. **13**, 995 (2023). https://doi.org/10.3390/cryst13070995

57. Martinez, S., Ortega, N., Celentano, D., Egea, A.J.S., Ukar, E., Lamikiz, A.: Analysis of the Part distortions for Inconel 718 SLM: A case study on the NIST test artifact. Mater. **13**, 5087 (2020). https://doi.org/10.3390/ma13225087

58. Sendino, S., Gardon, M., Lartategui, F., Martinez, S., Lamikiz, A.: The effect of the laser incidence angle in the surface of L-PBF processed parts. Coat. **10**, 1024 (2020). https://doi.org/10.3390/coatings10111024

59. Lesyk, D.A., Dzhemelinskyi, V.V., Martinez, S., Mordyuk, B.N., Lamikiz, A.: Surface shot peening post-processing of Inconel 718 alloy parts printed by laser powder bed fusion additive manufacturing. J. Mater. Eng. Perform. **30**, 6982–6995 (2021). https://doi.org/10.1007/s11665-021-06103-6

60. Mordyuk, B.N., Prokopenko, G.I.: Ultrasonic impact treatment–An effective method for nanostructuring the surface layers in metallic materials, in: M. Aliofhazraei Ed. Handbook of Mechanical Nanostructuring. 417–434 (2015). https://doi.org/10.1002/9783527674947.ch17

61. Lesyk, D.A., Martinez, S., Mordyuk, B.N., Dzhemelinskyi, V.V., Lamikiz, A., Prokopenko, G.I.: Effects of laser heat treatment combined with ultrasonic impact treatment on the surface topography and hardness of carbon steel AISI 1045. Optics Laser. Technol. **111**, 424–438 (2019). https://doi.org/10.1016/j.optlastec.2018.09.030

62. Evgeny, B., Hughes, T., Eskin, D.: Effect of surface roughness on corrosion behaviour of low carbon steel in inhibited 4 M hydrochloric acid under laminar and turbulent flow conditions. Corros. Sci. **103**, 196–205 (2016). https://doi.org/10.1016/j.corsci.2015.11.019

63. Grzesik, W.: Prediction of the functional performance of machined components based on surface topography: State of the art. J. Mater. Eng. Perform. **25**, 4460–4468 (2016). https://doi.org/10.1007/s11665-016-2293-z

64. To, D., Umezawa, O., Shinohara, T.: Detection of surface roughness evolution of carbon steel subjected to outdoor exposure and constant humidity corrosion tests. Mater. Trans. **59**, 1239–1243 (2018). https://doi.org/10.2320/matertrans.MF201702

65. Bergant, Z., Trdan, U., Grum, J.: Effect of high-temperature furnace treatment on the microstructure and corrosion behavior of NiCrBSi flame-sprayed coatings. Corros. Sci. **88**, 372–386 (2014). https://doi.org/10.1016/j.corsci.2014.07.057

66. Xia, D.-H., Deng, C.-M., Macdonald, D., Jamali, S., Mills, D., Luo, J.-L., Strebl, M.G., Amiri, M., Jin, W., Song, S., Hu, W.: Electrochemical measurements used for assessment of corrosion and protection of metallic materials in the field: A critical review. J. Mater. Sci. Technol. **112**, 151–183 (2022). https://doi.org/10.1016/j.jmst.2021.11.004

67. Trdan, U., Grum, J.: Evaluation of corrosion resistance of AA6082-T651 aluminium alloy after laser shock peening by means of cyclic polarisation and EIS methods. Corrosion Sci. **59**, 324–333 (2012). https://doi.org/10.1016/j.corsci.2012.03.019

68. Trdan, U., Hočevar, M., Gregorcic, P.: Transition from superhydrophilic to superhydrophobic state of laser textured stainless steel surface and its effect on corrosion resistance. Corros. Sci. **123**, 21–26 (2017). https://doi.org/10.1016/j.corsci.2017.04.005

69. Lesyk, D.A., Mordyuk, B.N., Martinez, S., Iefimov, M.O., Dzhemelinskyi, V.V., Lamikiz, A.: Influence of combined laser heat treatment and ultrasonic impact treatment on microstructure and corrosion behavior of AISI 1045 steel. Surf. Coat. Technol. **401**, 126275 (2020). https://doi.org/10.1016/j.surfcoat.2020.126275

70. Ailor, W.H. (ed.): Handbook on Corrosion testing and evaluation, p. 174. John Wiley and Sons Inc., New York (1971)

71. Popova, K., Prošek, T.: Corrosion monitoring in atmospheric conditions: A review. Metals. **12**, 171 (2022). https://doi.org/10.3390/met12020171

72. Bagherifard, S., Hickey, D.J., Fintova, S., Pastorek, F., Fernandez-Pariente, I., Bandini, M., Webster, T.J., Guagliano, M.: Effects of nanofeatures induced by severe shot peening (SSP) on mechanical,

corrosion and cytocompatibility properties of magnesium alloy AZ31. Acta Biomater. **66**, 93–108 (2018). https://doi.org/10.1016/j.actbio.2017.11.032

73. Jáquez-Muñoz, J.M., Gaona-Tiburcio, C., Cabral-Miramontes, J., Nieves-Mendoza, D., Maldonado-Bandala, E., Olguín-Coca, J., López-Léon, L.D., los Rios, J.P.F.-D., Almeraya-Calderón, F.: Electrochemical noise analysis of the corrosion of titanium alloys in NaCl and H2SO4 solutions. Metals. **11**, 105 (2021). https://doi.org/10.3390/met11010105

74. Toda, H., Minami, K., Koyama, K., Ichitani, K., Kobayashi, M., Uesugi, K., Suzuki, Y.: Healing behavior of preexisting hydrogen micropores in aluminum alloys during plastic deformation. Acta Mater. **57**, 4391–4403 (2009). https://doi.org/10.1016/j.actamat.2009.06.012

75. Dekhtyar, A.I., Mordyuk, B.N., Savvakin, D.G., Bondarchuk, V.I., Moiseeva, I.V., Khripta, N.I.: Enhanced fatigue behavior of powder metallurgy Ti–6Al–4V alloy by applying ultrasonic impact treatment. Mater. Sci. Eng. A. **641**, 348–359 (2015). https://doi.org/10.1016/j.msea.2015.06.072

76. Mordyuk, B.N., Prokopenko, G.I., Yu, P.V., L.E., Matokhnyuk, L.E., Byalonovich, A.V., Popova T.V.: Improved fatigue behavior of low-carbon steel 20GL by applying ultrasonic impact treatment combined with the electric discharge surface alloying. Mater. Sci. Eng. A **659**, 119–129 (2016). https://doi.org/10.1016/j.msea.2016.02.036

77. Yan, S., Wang, Y., Wang, Q., Zhang, C., Chen, D., Cui, G.: Enhancing mechanical properties of the spark plasma sintered Inconel 718 alloy by controlling the nano-scale precipitations. Mater. **12**, 3336 (2019). https://doi.org/10.3390/ma12203336

78. Lesyk, D.A., Martinez, S., Mordyuk, B.N., Pedash, O.O., Dzhemelinskyi, V.V., Lamikiz, A.: Comparison of effects of shot and ultrasonic peening treatments on surface properties of L-PBF-manufactured superalloy subjected to HIP combined with heat treatments. In: Post-processing techniques for additive manufacturing, pp. 207–243. Taylor & Francis (2023). https://doi.org/10.1201/9781003288619-9

79. Pariona, M.M., Teleginski, V., Santos, K.D., Machado, S., Zara, A.J., Zurba, N.K., Riva, R.: Yb-fiber laser beam effects on the surface modification of Al–Fe aerospace alloy obtaining weld filet structures, low fine porosity and corrosion resistance. Surf. Coat. Technol. **206**, 2293–2301 (2012). https://doi.org/10.1016/j.surfcoat.2011.10.007

80. Trdan, U., Grum, J.: SEM/EDS characterization of laser shock peening effect on localized corrosion of Al alloy in a near natural chloride environment. Corros. Sci. **82**, 328–338 (2014). https://doi.org/10.1016/j.corsci.2014.01.032

81. Finšgar, M., Fassbender, S., Nicolini, F., Milošev, I.: Polyethyleneimine as a corrosion inhibitor for ASTM 420 stainless steel in near-neutral saline media. Corros. Sci. **51**, 525–533 (2009). https://doi.org/10.1016/j.corsci.2008.12.006

82. Trueba, M., Trasatti, S.P.: Study of Al alloy corrosion in neutral NaCl by the pitting scan technique. Mater. Chem. Phys. **121**, 523–533 (2010). https://doi.org/10.1016/j.matchemphys.2010.02.022

Authors and Affiliations

**D. A. Lesyk[1,2,3] · B. N. Mordyuk[2] · S. Martinez[3] · V. V. Dzhemelinskyi[1] ·
D. Grzesiak[4] · D. Grochała[4] · A. Lamikiz[3,5]**

✉ D. A. Lesyk
   lesyk_d@ukr.net

✉ B. N. Mordyuk
   mordyuk@imp.kiev.ua

[1] Laser Systems and Advanced Technologies Department, National Technical University
    of Ukraine "Igor Sikorsky Kyiv Polytechnic Institute", 37 Prospect Beresteiskyi, Kyiv 03056,
    Ukraine

[2] Physical Principles for Surface Engineering Department, Kurdyumov Institute for Metal Physics
    of the NAS of Ukraine, 36 Academician Vernadsky Blvd., Kyiv 03142, Ukraine

[3] Aeronautics Advanced Manufacturing Center, University of the Basque Country, 202 Bizkaia
    Science and Technology Park, 48170 Zamudio, Spain

[4] Mechanical Engineering and Mechatronics Department, West Pomeranian University
    of Technology, 17 Aleja Piastow, 70310 Szczecin, Poland

[5] Mechanical Engineering Department, University of the Basque Country, Alameda Urquijo S/N,
    48013 Bilbao, Spain